

IN SEARCH OF EXTRATERRESTRIAL HIGH ENERGY NEUTRINOS

LUIS A. ANCHORDOQUI

*Department of Physics,
University of Wisconsin-Milwaukee, Milwaukee WI 53201, USA*

TERESA MONTARULI

*Department of Physics,
University of Wisconsin-Madison, Madison WI 53706, USA*

Key Words neutrino telescopes, cosmic rays, dark matter

Abstract In this paper we review the search for astrophysical neutrinos. We begin by summarizing the various theoretical predictions which correlate the expected neutrino flux with data from other messengers, specifically gammas and ultra-high energy cosmic rays. We then review the status and results of neutrino telescopes in operation and decommissioned, the methods used for data analysis and background discrimination. Particular attention is devoted to the challenge enforced by the highly uncertain atmospheric muon and neutrino backgrounds in relation to searches of diffuse neutrino fluxes. Next, we examine the impact of existing limits on neutrino fluxes on studies of the chemical composition of cosmic rays. After that, we show that not only do neutrinos have the potential to discover astrophysical sources, but the huge statistics of atmospheric muons can be a powerful tool as well. We end by discussing the prospects for indirect detection of dark matter with neutrino telescopes.

CONTENTS

INTRODUCTION	2
COSMIC RAY \rightleftharpoons NEUTRINO CONNECTION	3
NEUTRINO TELESCOPES	10
<i>Detection principle</i>	10
<i>Detectors in operation and decommissioned</i>	13
EXPERIMENTAL RESULTS AND SCIENTIFIC IMPACT	17
<i>Steady and flaring point-source searches</i>	18
<i>Atmospheric muons and neutrinos</i>	19
<i>Searches for diffuse cosmic neutrino fluxes</i>	22
<i>Cosmic ray proton fraction</i>	23
<i>Dark matter searches</i>	24
CONCLUSIONS AND FUTURE PROSPECTS	27

1 INTRODUCTION

It has long been recognized that high energy protons produced in cosmic ray accelerators would also generate an observable flux of cosmic neutrinos, mainly through charged pion production in collisions with the ambient gas or with radiation fields (1). Viceversa, the emission of neutrinos necessarily implies the existence of relativistic baryons, and consequently the acceleration of cosmic rays. Upcoming catalogues of cosmic ray and neutrino sources would thus in principle be identical were it not for the different properties of the messengers themselves.

Neutrinos can escape from the innermost regions of galaxies where light and other kinds of electromagnetic radiation are blocked by matter and hence can be tracers of processes which stay hidden to traditional photon astronomy. Furthermore, neutrinos carry with them information about the site and circumstances of their production. Undelected and unabsorbed they can point back to very distant sources, resolving the origin of the highest energy cosmic rays and the underlying acceleration mechanism. Besides, unlike gamma-rays that can be produced via synchrotron radiation, or inverse Compton scattering, neutrinos provide incontrovertible evidence for acceleration of baryonic cosmic rays.

MeV neutrino astronomy has been possible for about 45 years (2). Thus far two sources of non-atmospheric neutrinos have been identified: the Sun (3) and SN1987a (4). During the next decade we will be able to observe the universe using high energy “neutrino light.” This will doubtless illuminate a wondrous new view of the universe.

Candidate sources of high-energy neutrinos are of both galactic and extra-galactic varieties, the latter being expected to dominate at the highest energies just as for the parent cosmic rays. Energy balance considerations suggest that the diffuse galactic flux of neutrinos predominantly originates in supernova remnants (5). Dense molecular clouds, often found in star forming regions where the supernovae (SNe) explode, are particularly efficient at converting protons into pions that decay into gamma rays and neutrinos (6). Other possibilities for galactic sources include microquasars (7), γ -ray binaries (8), and pulsar wind nebulae (9). By far, the most likely extra-galactic sources are active galactic nuclei (AGN) (12) and gamma-ray bursts (GRBs) (13). [For reviews see e.g., (10) and for neutrino flux estimates see (11)]. In addition, the so-called cosmogenic neutrinos are guaranteed to exist, their amount being still highly uncertain. These originate from the decay of charged pions produced in the interactions of protons with the isotropic photon background (14–16).

As for conventional astronomy, neutrino astronomers observe the neutrino sky through the atmosphere. This is a curse and a blessing; the background of neutrinos produced by cosmic rays in interactions with air nuclei provides a beam essential for calibrating the detectors and demonstrating the neutrino measurement technique. It also provides an opportunity to probe neutrino standard oscillations and those arising from new physics, such as violation of Lorentz invariance (17). Especially unique is the energy range of the atmospheric neutrino beam between 10^4 GeV $\lesssim E_\nu \lesssim 10^8$ GeV, not within reach of accelerators, that may reveal the existence of neutrinos from prompt decays of charmed mesons and

baryons (18). Over the next decade, a data set of the order of one million atmospheric neutrinos will be collected. The statistics will be so large that mapping of the Earth's interior will be possible via neutrino tomography (19).

Though neutrino astrophysics is the central motivation to build neutrino telescopes, ultrahigh energy cosmic neutrinos are also unique probes of new physics as their interactions are uncluttered by the strong and electromagnetic forces and can reach center-of-mass energies of $\sqrt{s} \sim 245$ TeV (20). Rates for new physics processes, however, are difficult to test since the flux of cosmic neutrinos is virtually unknown. It is possible to mitigate this by using multiple observables which allow one to decouple effects of the flux and cross section (21). Large neutrino telescopes may also open a new perspective for indirect searches of dark matter by detecting neutrinos produced via annihilation of weakly interactive massive particles trapped within the Sun, or at the center of the Earth (22).

The layout of the paper is as follows: in Sec. 2 we overview the connection between cosmic ray observations and expected neutrino fluxes; in Sec. 3 we review the status of neutrino telescope construction, operation and data analysis; in Sec. 4 we analyze the upper limits on neutrino fluxes set by the different experiments to assess their scientific impact; in Sec. 5 we provide a summary and discuss future prospects.

2 COSMIC RAY \rightleftharpoons NEUTRINO CONNECTION

The cosmic ray flux falls as an approximate power-law in energy, $J_{\text{CR}}(E) \propto E^{-\alpha}$, with $\alpha \simeq 2.7$ from about 10 GeV up to the 'knee' in the spectrum at $E \sim 3 \times 10^6$ GeV where it steepens to $\alpha \simeq 3.1$; it then steepens further to $\alpha \simeq 3.25$ at $E \sim 4 \times 10^8$ GeV (the so called 'dip') and flattens back to $\alpha \simeq 2.69$ at $E \sim 3 \times 10^9$ GeV, the so-called 'ankle' (23). The spectrum extends up to at least $E \sim 10^{11}$ GeV with a steep spectrum ($\alpha \simeq 4.2$) beyond $E = 5 \times 10^{10}$ GeV (24), in accord with the prediction by Greisen, Zatsepin and Kuz'min (GZK) (25).

The energy density associated with the flux of galactic cosmic rays is $\rho_E \sim 10^{-12}$ erg cm $^{-3}$ (26). This is about the value of the corresponding energy density $B^2/8\pi$ of the microgauss magnetic field in the Galaxy. Given that the average containment time of the cosmic rays in our Galaxy is $\sim 3 \times 10^6$ yr, the power needed to maintain this energy density is $\sim 10^{-26}$ erg/cm 3 s. For a nominal volume of the galactic disk of 10^{67} cm 3 this requires an accelerator delivering power of about 10^{41} erg/s. This happens to be 10% of the power produced by supernovae, releasing 10^{51} erg every 30 yr. This coincidence is the basis for the idea that shocks produced by supernovae expanding into the interstellar medium are the origin of the galactic cosmic rays.

The conversion of 10^{50} erg of energy into particle acceleration is believed to occur by diffusive shock acceleration in the young ($10^3 - 10^4$ yr) SN remnant expanding into the interstellar medium. If high energy cosmic rays are indeed associated with the remnant, they will interact with hydrogen atoms in the interstellar medium to produce pions that decay into roughly equal numbers of photons and neutrinos: the former via $\pi^0 \rightarrow \gamma\gamma$, the latter via $\pi^+ \rightarrow e^+ \nu_e \nu_\mu \bar{\nu}_\mu$ (and the conjugate process). These may provide us with indirect evidence for

cosmic ray acceleration. The observation of these pionic gamma rays has been one of the motivations for neutrino astronomy as well as, to a large extent, for gamma-ray astronomy.

Whereas the details are complex and predictions can be treacherous, a simple estimate of the gamma ray flux associated with a supernova remnant can be made following Aharonian, Drury and Volk (27). The emissivity in pionic gamma rays is simply proportional to the density of cosmic rays for energy in excess of 1 TeV, $n_{\text{CR}}(> 1 \text{ TeV}) \simeq 4 \times 10^{-14} \text{ cm}^{-3}$, and to the target density of hydrogen atoms, n_{H} . The proportionality factor is determined by particle physics.

The emissivity (number/volume/time/energy) of neutral pions resulting from an isotropic distribution of highly relativistic particles following a power-law energy spectrum $dn_{\text{CR}}(E_N)/dE_N \propto E_N^{-\alpha}$ is given by

$$Q_{\pi}(E_{\pi}) = c n_{\text{H}} \int_{E_N^{\text{th}}(E_{\pi})}^{E_N^{\text{max}}} \frac{dn_{\text{CR}}(E_N)}{dE_N} \frac{d\sigma_A}{dE_{\pi}}(E_{\pi}, E_N) dE_N \quad (1)$$

where $E_N^{\text{th}}(E_{\pi})$ is the minimum energy per nucleon required to produce a pion with energy E_{π} , and $d\sigma_A(E_{\pi}, E_N)/dE_{\pi}$ is the differential cross section for the production of a pion with energy E_{π} in the lab frame due to the collision of a nucleus A of energy per nucleon E_N with a hydrogen atom at rest. The differential cross-section can be parametrized by

$$\frac{d\sigma_A}{dE_{\pi}}(E_{\pi}, E_N) \simeq \frac{\sigma_0^A}{E_{\pi}} x F_{\pi}(x, E_N), \quad (2)$$

where $x \equiv E_{\pi}/E_N$, $\sigma_0^A = A^{2/3} \sigma_0$ (with $\sigma_0 \simeq 40 \text{ mb}$) provides a scaling of the cross-section with the atomic mass number (26), and $F_{\pi}(x, E_N)$ is a fragmentation function. Taking into account that inelastic hadronic collisions lead to roughly equal numbers of π^0 , π^+ , and π^- mesons, as well as the mild variation with pseudorapidity, the parametrization (28)

$$F_{\pi}(x, E_N) = 4\beta B_{\pi} x^{\beta-1} \left(\frac{1-x^{\beta}}{1+r x^{\beta}(1-x^{\beta})} \right)^4 \left(\frac{1}{1-x^{\beta}} + \frac{r(1-2x^{\beta})}{1+r x^{\beta}(1-x^{\beta})} \right) \times \left(1 - \frac{m_{\pi}}{xE_N} \right)^{1/2}, \quad (3)$$

is found (29) to be consistent at 1σ level with data collected at the Tevatron by the CDF detector (30); $B_{\pi} = a + 0.25$, $\beta = 0.98/\sqrt{a}$, $r = 2.6/\sqrt{a}$, $a = 3.67 + 0.83L + 0.075L^2$, and $L = \ln(E_N/\text{TeV})$. Substitution of Eq. (2) into Eq. (1) leads to

$$Q_{\pi}(E_{\pi}) \simeq Z_{A\pi}(\alpha) Q_A^{\text{AH}}(E_{\pi}) \quad (4)$$

where

$$Q_A^{\text{AH}}(E_N) = \sigma_0^A c n_{\text{H}} \frac{dn_{\text{CR}}}{dE_N}(E_N) \quad (5)$$

and the spectrum-weighted moment of the inclusive cross-section or so-called Z -factor is given by

$$Z_{A\pi}(\alpha) \equiv \int_0^1 x^{\alpha-1} F(x, E_N) dx. \quad (6)$$

On average, the photons carry one-half of the energy of the pion, and thus the γ -ray emissivity is

$$\begin{aligned} Q_\gamma^{Ap}(E_\gamma) &= 2 \int_{E_\pi^{\min}(E_\gamma)}^{E_\pi^{\max}} \frac{Q_\pi^{Ap}(E_\pi)}{(E_\pi^2 - m_\pi^2)^{1/2}} dE_\pi \\ &\simeq Z_{\pi\gamma}(\alpha) Q_\pi^{Ap}(E_\gamma), \end{aligned} \quad (7)$$

where $E_\pi^{\min}(E_\gamma) = E_\gamma + m_\pi^2/(4E_\gamma)$ and $Z_{\pi\gamma}(\alpha) = 2/\alpha$. Assuming proton dominance and emission spectrum $\propto E_N^{-2}$, the gamma ray emissivity above 1 TeV becomes

$$\begin{aligned} Q_\gamma(> 1 \text{ TeV}) &= c \langle E_\pi/E_N \rangle \sigma_0 n_H n_{\text{CR}}(> 1 \text{ TeV}) \\ &\simeq 10^{-29} \left(\frac{n_H}{\text{cm}^{-3}} \right) \frac{\text{photons}}{\text{cm}^3 \text{ s}}, \end{aligned} \quad (8)$$

where $\langle E_\pi/E_N \rangle \sim 0.2$ is the average energy of the secondary pions relative to the cosmic ray protons. For different spectral indices, the quantity $\langle E_\pi/E_N \rangle$ is generalized to the spectrum-weighted moments for pion production by nucleons given in Eq. (6).

The density of protons from a supernova converting a total kinetic energy W of 10^{50} erg to proton acceleration is approximately given by ρ/W , where we will assume that the density in the remnant is not very different from the ambient energy density $\rho_E \sim 10^{-12}$ erg cm $^{-3}$ of galactic cosmic rays. This approximation is valid for young remnants in their Sedov phase (31). The total luminosity in gamma rays is then

$$\mathcal{L}_\gamma(> 1 \text{ TeV}) = Q_\gamma \frac{W}{\rho_E} \simeq 10^{33} \text{ photons s}^{-1}. \quad (9)$$

The expected rate of TeV photons from a supernova at a distance $d \sim 1$ kpc is

$$\begin{aligned} \frac{d\mathcal{N}_\gamma}{d(\ln E_\gamma)}(> 1 \text{ TeV}) &= \frac{\mathcal{L}_\gamma}{4\pi d^2} \\ &\simeq 10^{-11} \left(\frac{\text{photons}}{\text{cm}^2 \text{ s}} \right) \left(\frac{W}{10^{50} \text{ erg}} \right) \left(\frac{n_H}{\text{cm}^{-3}} \right) \left(\frac{\text{kpc}}{d} \right)^2. \end{aligned} \quad (10)$$

Neglecting absorption effects, the all flavor neutrino and photon fluxes are roughly equal, and so we anticipate an event rate of 3 detected neutrinos per decade of energy per km 2 yr, a result readily obtained from the relation

$$\frac{d\mathcal{N}_\nu}{d(\ln E_\nu)}(> 1 \text{ TeV}) \simeq 10^{-11} \left(\frac{\text{neutrinos}}{\text{cm}^2 \text{ s}} \right) \left(\frac{\text{area}}{1 \text{ km}^2} \right) \left(\frac{\text{time}}{1 \text{ yr}} \right) P_\nu, \quad (11)$$

where the last factor indicates the average probability for neutrino detection; for the TeV energy considered here $P_\nu \sim 10^{-6}$ (1).

This estimate may be somewhat optimistic because we assumed that the neutrino energy reaches 100 TeV with an E_ν^{-2} spectrum.¹ On the other hand, if the

¹Such a spectral index is typical of Fermi acceleration mechanisms (32).

galactic cosmic ray spectrum extends at least up to the knee ($E \sim 3000$ TeV), then some of the sources must produce ~ 100 TeV secondaries.

Photo-disintegration of high-energy nuclei, followed by prompt photo-emission from the excited daughter nuclei also produces TeV gamma rays and antineutrinos. In this chain reaction, the nuclei act in analogy to Einstein’s relativistic moving mirror to “double-boost” eV starlight to TeV energies for a Lorentz boost factor $> 10^6$ (33). The TeV antineutrino counterpart is produced through β -decay of the emitted neutrons (34). Effective nucleus photo-disintegration is expected in stellar associations harboring a large population of massive and early type stars that can provide the required Lyman- α emission. Directional beams of galactic antineutrinos and gamma rays may thus emerge as fluctuations over the diffuse intensity.

A plethora of explanations have been proposed to address the production mechanism of cosmic rays beyond the dip (35). In the absence of a single model which is consistent with all data, the origin of these particles remains a mystery. Clues to solve the mystery are not immediately forthcoming from the data, particularly since various experiments report mutually inconsistent results. In recent years, a somewhat confused picture regarding the nature of these cosmic rays has been emerging. The HiRes data have been interpreted as a change in cosmic ray composition, from heavy nuclei to protons, at $E \sim 4 \times 10^8$ GeV (36). This is an order of magnitude lower in energy than the previous crossover deduced from the Fly’s Eye data (37).

The end-point of the galactic flux is expected to be dominated by iron, as the large charge Ze of heavy nuclei reduces their Larmor radius (containment scales linearly with Z) and facilitates their acceleration to highest energy (again scaling linearly with Z). The dominance of nuclei in the high energy region of the galactic flux carries the implication that any changeover to protons represents the onset of dominance by an extra-galactic component. The inference from this HiRes data is therefore that the extra-galactic flux is beginning to dominate the galactic flux already at $E \sim 4 \times 10^8$ GeV. Such a transition would appear to require considerable fine-tuning of the shape and normalization of the two spectra. It has been argued however that the spectral shape required for the extra-galactic component can develop naturally during the propagation of extra-galactic protons in the cosmic microwave background (CMB) over cosmological distances (38). At $E \sim 3 \times 10^8$ GeV the energy losses due to e^+e^- pair production and cosmic expansion are roughly equal and thus produce a steepening of an initially featureless power-law injection spectrum. Significantly, the onset of the extra-galactic component would be well below $E_{\text{GZK}} \sim 5 \times 10^{10}$ GeV, the threshold energy for resonant $p\gamma_{\text{CMB}} \rightarrow \Delta^+ \rightarrow N\pi$ energy-loss on the CMB, and so samples sources even at large redshift.

It is helpful to envision the cosmic ray engines as machines where protons are accelerated and (possibly) permanently confined by the magnetic fields of the acceleration region. The production of neutrons and pions and subsequent decay produces neutrinos, gamma rays, and cosmic rays. If the neutrino-emitting source also produces high energy cosmic rays, then pion production must be the principal agent for the high energy cutoff on the proton spectrum. Conversely,

since the protons must undergo sufficient acceleration, inelastic pion production needs to be small below the cutoff energy; consequently, the plasma must be optically thin. Since the interaction time for protons is greatly increased over that of neutrons because of magnetic confinement, the neutrons escape before interacting, and on decay give rise to the observed cosmic ray flux. The foregoing can be summarized as three conditions on the characteristic nucleon interaction time scale τ_{int} ; the neutron decay lifetime τ_n ; the characteristic cycle time of confinement τ_{cycle} ; and the total proton confinement time τ_{conf} : (i) $\tau_{\text{int}} \gg \tau_{\text{cycle}}$; (ii) $\tau_n > \tau_{\text{cycle}}$; (iii) $\tau_{\text{int}} \ll \tau_{\text{conf}}$. The first condition ensures that the protons attain sufficient energy. Conditions (i) and (ii) allow the neutrons to escape the source before decaying. Condition (iii) permits sufficient interaction to produce neutrons and neutrinos. These three conditions together define an optically thin source (39). A desirable property to reproduce the almost structureless energy spectrum is that a single type of source will produce cosmic rays with a smooth spectrum across a wide range of energy.

The cosmic ray flux above the ankle is often summarized as “one 3×10^{10} GeV particle per kilometer square per year per steradian.” This can be translated into an energy flux (41)

$$\begin{aligned}
 E \{E J_{\text{CR}}\} &= \frac{3 \times 10^{10} \text{ GeV}}{(10^{10} \text{ cm}^2)(3 \times 10^7 \text{ s}) \text{ sr}} \\
 &= 10^{-7} \text{ GeV cm}^{-2} \text{ s}^{-1} \text{ sr}^{-1}.
 \end{aligned} \tag{12}$$

From this we can derive the energy density ρ_E in ultra-high energy cosmic rays using flux = velocity \times density, or

$$4\pi \int dE \{E J_{\text{CR}}\} = c\rho_E. \tag{13}$$

This leads to

$$\rho_E = \frac{4\pi}{c} \int_{E_{\text{min}}}^{E_{\text{max}}} \frac{10^{-7}}{E} dE \frac{\text{GeV}}{\text{cm}^3} \simeq 3 \times 10^{-19} \frac{\text{TeV}}{\text{cm}^3}, \tag{14}$$

taking the extreme energies of the accelerator(s) to be $E_{\text{max}}/E_{\text{min}} \simeq 10^3$. The power required for a population of sources to generate this energy density over the Hubble time of 10^{10} yr is

$$E^2 \frac{d\dot{N}_{\text{CR}}}{dE} \Bigg|_{E_{\text{min}}} = \frac{\dot{\epsilon}_{\text{CR}}^{[10^{19}, 10^{21}]}}{\ln(10^{21}/10^{19})} \approx 10^{44} \text{ erg Mpc}^{-3} \text{ yr}^{-1}, \tag{15}$$

where an energy spectrum $\propto E^{-2}$ has been assumed (40).

This works out to about 3×10^{39} erg s $^{-1}$ per galaxy, 3×10^{42} erg s $^{-1}$ per cluster of galaxies, $\sim 2 \times 10^{44}$ erg s $^{-1}$ per active galaxy, or $\sim 2 \times 10^{52}$ erg per cosmological gamma ray burst (41). The coincidence between these numbers and the observed output in electromagnetic energy of these sources explains why they have emerged as the leading candidates for the cosmic ray accelerators. The coincidence is consistent with the relationship between cosmic rays and photons built into the previously discussed “optically thin” source.

The energy density of neutrinos produced through $p\gamma$ interactions of these protons can be directly tied to the injection rate of cosmic rays

$$E_\nu^2 \frac{dN_\nu}{dE_\nu} \approx \frac{3}{8} \epsilon_\pi t_H E^2 \frac{d\dot{N}_{\text{CR}}}{dE}, \quad (16)$$

where t_H is the Hubble time and ϵ_π is the fraction of the energy which is injected in protons lost into photo-pion interactions. (The factor of $3/8$ comes from the fact that, close to threshold, roughly half the pions produced are neutral, thus not generating neutrinos, and one quarter of the energy of charged pion decays goes to electrons rather than neutrinos.)² The ‘‘Waxman-Bahcall bound’’ is defined by the condition $\epsilon_\pi = 1$

$$\begin{aligned} [E_\nu^2 \Phi_\nu]_{\text{WB}} &\approx (3/8) \xi_Z \epsilon_\pi t_H \frac{c}{4\pi} E^2 \frac{d\dot{N}_{\text{CR}}}{dE} \\ &\approx 2.3 \times 10^{-8} \epsilon_\pi \xi_Z \text{ GeV cm}^{-2} \text{ s}^{-1} \text{ sr}^{-1}, \end{aligned} \quad (17)$$

where the parameter ξ_Z accounts for the effects of source evolution with redshift, and is expected to be ~ 3 (42). For interactions with the ambient gas (i.e., pp rather than $p\gamma$ collisions), the average fraction of the total pion energy carried by charged pions is about $2/3$, compared to $1/2$ in the photo-pion channel. In this case, the upper bound given in Eq. (17) is enhanced by 33% (43).

The actual value of the neutrino flux depends on what fraction of the proton energy is converted to charged pions (which then decay to neutrinos). To quantify this, we follow Waxman-Bahcall and define ϵ_π as the ratio of charged pion energy to the *emerging* nucleon energy at the source. For resonant photoproduction, the inelasticity is kinematically determined by requiring equal boosts for the decay products of the Δ^+ (44), giving $\epsilon_\pi = E_{\pi^+}/E_n \approx 0.28$, where E_{π^+} and E_n are the emerging charged pion and neutron energies, respectively. For $pp \rightarrow NN + \text{pions}$, where N indicates a final state nucleon, the inelasticity is ≈ 0.6 (45). This then implies that the energy carried away by charged pions is about equal to the emerging nucleon energy, yielding (with our definition) $\epsilon_\pi \approx 1$.

At production, if all muons decay, the neutrino flux consists of equal fractions of ν_e , ν_μ and $\bar{\nu}_\mu$. Originally, the Waxman-Bahcall bound was presented for the sum of ν_μ and $\bar{\nu}_\mu$ (neglecting ν_e), motivated by the fact that only muon neutrinos are detectable as track events in neutrino telescopes. Since oscillations in the neutrino sector mix the different species, we chose instead to discuss the sum of all neutrino flavors. When the effects of oscillations are accounted for, *nearly* equal numbers of the three neutrino flavors are expected at Earth (46). (For a detailed calculation of the flavor ratios see e.g., (47).)

If the injected cosmic rays include nuclei heavier than protons, then the neutrino flux expected from the cosmic ray sources may be modified. Nuclei undergoing acceleration can produce pions, just as protons do, through interactions with the ambient gas, so the Waxman-Bahcall argument would be unchanged in

²The average neutrino energy from the direct pion decay is $\langle E_{\nu_\mu} \rangle^\pi = (1-r) E_\pi/2 \simeq 0.22 E_\pi$ and that of the muon is $\langle E_\mu \rangle^\pi = (1+r) E_\pi/2 \simeq 0.78 E_\pi$, where r is the ratio of muon to the pion mass squared. In muon decay, since the ν_μ has about $1/3$ of its parent energy, the average muon neutrino energy is $\langle E_{\nu_\mu} \rangle^\mu = (1+r) E_\pi/6 = 0.26 E_\pi$.

this case. However, if interactions with radiation fields dominate over interactions with matter, the neutrino flux would be suppressed if the cosmic rays are heavy nuclei. This is because the photo-disintegration of nuclei dominates over pion production at all but the very highest energies. Defining κ as the fraction of nuclei heavier than protons in the observed cosmic ray spectrum, the resulting neutrino flux is then given by

$$E_\nu^2 J_\nu \approx (1 - \kappa) [E_\nu^2 \Phi_\nu]_{\text{WB}} . \quad (18)$$

Unfortunately, current observations do not allow a conclusive determination of κ . For $1.6 \leq \alpha \leq 2.1$, the data can be well reproduced if the emitted cosmic rays consist entirely of nuclei with masses in the intermediate (carbon, nitrogen, or oxygen) to heavy (iron, silicon) range, but a mixture of protons (97%) and heavier species (3%) is also acceptable (16, 48).

The diffuse neutrino flux has an additional component originating in the energy losses of ultra-high energy cosmic rays *en route* to Earth. Ultrahigh energy protons above the ‘‘GZK cutoff’’ interact with the cosmic microwave and infrared backgrounds as they propagate over cosmological distances. These interactions generate pions and neutrons, which decay to produce neutrinos (14). The accumulation of these neutrinos over cosmological time is known as the cosmogenic neutrino flux. Ultra-high energy nuclei also interact with the cosmic microwave and infrared backgrounds, undergoing photodisintegration. The disassociated nucleons then interact with the cosmic microwave and infrared backgrounds to produce cosmogenic neutrinos (49). In the limit that the cosmic backgrounds are opaque to cosmic ray nuclei, full disintegration occurs and the resulting cosmogenic neutrino spectrum is not dramatically different from that predicted in the all-proton case (assuming the cosmic ray spectrum extends to high enough energies to produce protons above the GZK cutoff). In contrast, if a significant fraction of cosmic ray nuclei remain intact, the resulting flux of cosmogenic neutrinos can be considerably suppressed. Of course, the predicted neutrino flux also depends on the spectrum, the source evolution, and the nature of the emitted cosmic rays (14–16). Representative spectra of cosmogenic neutrinos are shown in Fig. 1, for pure Fe and bi-modal Fe + p mass compositions consistent with data (16). The estimates shown in Fig. 1 are framed in the context of the usual concordance cosmology (50) of a flat universe dominated by a cosmological constant with $\Omega_\Lambda \sim 0.7$, the rest being cold dark matter (CDM) with $\Omega_m \sim 0.3$. (A rigorous compilation of the Λ CDM parameters is provided in Sec. 4.5.) The Hubble parameter is given by $H^2(z) = H_0^2 (\Omega_m (1+z)^3 + \Omega_\Lambda)$, normalized to its value today of $70 \text{ km s}^{-1} \text{ Mpc}^{-1}$. The time-dependence of the red-shift can be expressed via $dz = -dt (1+z)H$. The cosmological evolution of the source density per co-moving volume is parameterized as

$$\mathcal{L}_i(z, E) = \mathcal{H}(z) \mathcal{L}_i(0, E) , \quad (19)$$

where $\mathcal{H}(z)$ is the cosmological evolution of the cosmic ray sources, which is taken here to follow the luminosity density evolution of QSOs: $\mathcal{H}_{\text{QSO}}(z) = (1+z)^3$, for $z < 1.9$, $\mathcal{H}_{\text{QSO}}(z) = (1+1.9)^3$ for $1.9 < z < 2.7$, and $\mathcal{H}(z) = (1+1.9)^3 \exp\{(2.7-z)/2.7\}$, for $z > 2.7$ (15). For such a cosmological evolution, which is similar to that describing the star formation rate, $\xi_Z \approx 3$ (42).

In summary, the case for doing high energy neutrino astronomy is compelling; the challenge is to deliver the technology to build a neutrino detector with the largest possible effective area and the best possible angular and energy resolution sensitive to these cosmic neutrino fluxes. We discuss this next.

3 NEUTRINO TELESCOPES

3.1 Detection principle

It took about 35 years between Markov's conception of the Neutrino Telescope (NT) detection principle (51) to the operation of the first full detector. Though NTs use the well established technique of photomultipliers (PMTs), they are challenging instruments to build. The difficulties for construction arise from *(i)* the necessity of instrumenting extremely large regions, mainly because of the smallness of the neutrino-nucleon cross section and the steeply decreasing energy spectrum of neutrino fluxes of atmospheric and astrophysical origin; *(ii)* the required darkness and transparency of the medium to detect the faint Cherenkov light produced by ultra-relativistic charged particles; and *(iii)* the need for filtering neutrino events out of the more abundant atmospheric muons. Detectors are located under 1 – 4 km of water or ice, where, for $E_\nu \gtrsim 100$ GeV, the downward-going background of atmospheric muons is about 5 – 6 orders of magnitude larger than the atmospheric neutrino flux coming from all directions (see Figs. 2 and 3).

NTs are tridimensional matrices of photodetectors made of strings of optical modules (OMs) that house large photocathode PMTs and protect them from both the water column pressure (when they are installed in the sea or in lakes) and the pressure during ice refreezing (for Antarctic detectors). In some cases OMs also comprise front-end electronics. The NT energy threshold depends on the vertical spacing between PMTs and the horizontal distance of strings; typical values range between 50 GeV to 1 TeV. The threshold is not sharp, but the detection efficiency increases with energy. Neutrinos interact with the medium nuclei in and around the detector through charged ($\nu_{\text{lepton}} + X \rightarrow \text{lepton} + X$) and neutral ($\nu_{\text{lepton}} + X \rightarrow \nu_{\text{lepton}} + X$) current interactions. Charged current deep inelastic collisions above 10 GeV dominate over all other processes with the exception of $\bar{\nu}_e e$ interactions, because of the intermediate-boson resonance formed in the neighborhood of $E_\nu^{\text{res}} = M_W^2/2m_e \approx 6.3 \times 10^6$ GeV, generally referred to as the Glashow resonance (62). The resonant reactions $\bar{\nu}_e e^- \rightarrow W^- \rightarrow \bar{\nu}_\mu \mu^-$ and $\bar{\nu}_e e^- \rightarrow W^- \rightarrow \text{hadrons}$ may offer a detectable signal if the $\bar{\nu}_e$ flux originates in pp collisions (43).³ The neutrino-nucleon cross section rises almost linearly with energy (63). This implies that *(i)* the interaction probability increases with energy, indicating that NTs are optimal detectors at high energies, and *(ii)* neutrinos begin to be absorbed in the Earth. The shadowing effect of the Earth not only depends on the neutrino energy but also on the incident zenith angle (64).

³In pp collisions the nearly isotopically neutral mix of pions will create on decay a neutrino population in the ratio $N_{\nu_\mu} = N_{\bar{\nu}_\mu} = 2N_{\nu_e} = 2N_{\bar{\nu}_e}$. In contrast, photopion interactions leave the isotopically asymmetric process $p\gamma \rightarrow \Delta^+ \rightarrow \pi^+ n$ as the dominant source of neutrinos; then, at production, $N_{\nu_\mu} = N_{\bar{\nu}_\mu} = N_{\nu_e} \gg N_{\bar{\nu}_e}$.

At about 10^5 GeV, the interaction length of muon and electron neutrinos is about the Earth's diameter, and hence about 80% (40%) of the neutrinos with $\cos\theta = -1$ (-0.7) are absorbed, where θ is the zenith angle. Hence, this indicates that at very high energy, where it is expected that the astrophysical signal emerges from the atmospheric muon and neutrino backgrounds, detectors should have a large acceptance. There is a completely different behavior for tau neutrinos. In propagating through the Earth, they interact producing tau-leptons that decay back into a ν_τ of lower energy in what is referred to as a "regeneration effect" (65). The two leptonic channels, with a branching fraction of about 17%, produce also ν_e and ν_μ . The relevance of this phenomenon in terms of event rates at detectors depends on the neutrino spectrum.

NTs detect ultra-relativistic ($\beta \sim 1$) secondary particles produced in the interaction of the incoming neutrino with an atomic nucleus. These particles, which typically travel faster than the speed of light in the detector medium, emit directional Cherenkov light at an angle $\theta_C = \cos^{-1} [1/\beta n] \sim 41^\circ$, where n is the refraction index of the medium. Between 300-600 nm, the region where PMTs are mostly sensitive, about 3.2×10^4 Cherenkov photons are emitted by a bare muon track in the ice per meter. Once the OM acceptance and PMT quantum efficiency are accounted for, on average only 6% of these photons contribute to the signal. The muon neutrino event topology is very different from that of electron and tau neutrinos. Secondary muons travel long distances and can be reconstructed with an angular resolution better than a degree at high energy. Namely, the kinematic angle between the muon and the neutrino in the deep inelastic regime ($\gtrsim 10$ GeV) decreases with neutrino energy as $\sqrt{\langle\theta_{\nu\mu}^2\rangle} \propto \sqrt{m_p/E_\nu}$ (26), with m_p the proton mass. For $E_\nu \gtrsim 10$ TeV, the angle becomes negligible with respect to the intrinsic detector resolution. NTs measure the leading edge time of the PMT signal and in some cases the fully digitized waveform and the integrated charge. This information is used to reconstruct tracks for muons that travel long distances across the detector and determine their energy as well. Charged current (CC) interactions of electron and tau neutrinos and all flavor neutral current (NC) interactions produce cascade-like events. The resulting hadronic and electromagnetic showers are small with respect to the scale of the separation between OMs, and so they are almost a point-like source of light that propagates with some anisotropy that remembers the direction of the incoming neutrino. This prevents the achievement of an angular resolution for neutrinos comparable to the muon channel.

Muons lose energy according to

$$\frac{dE_\mu}{dx} = -a - bE_\mu, \quad (20)$$

where $a = 2.0 \times 10^{-6}$ TeV cm²/g is the continuous ionization term. The stochastic energy loss term bE , with $b = 4.2 \times 10^{-6}$ cm²/g (50), dominates at energies $\gtrsim 1$ TeV in water or ice. The distance a muon travels before its energy drops below some energy threshold E_μ^{th} , called the muon range, is then given by

$$\lambda_\mu = \frac{1}{b} \ln \left[\frac{a + bE_\mu}{a + bE_\mu^{\text{th}}} \right]. \quad (21)$$

For muons with $E_\mu > 1$ TeV propagating in water or ice, stochastic losses, such as bremsstrahlung, pair production, and photonuclear processes (bE_μ term) dominate over the ionization constant a term. In the first kilometer, a muon of about 100 TeV typically loses energy in 2 – 3 showers carrying more than 10% of its initial energy. Near the end of its range the muon becomes a minimum ionizing particle emitting light that creates single photoelectron signals at a distance of just over 10 m from the track. Above 1 TeV, the muon energy can be reconstructed with an energy resolution in $\log_{10}E_\mu$ of about 0.3. Of course, above a certain energy saturation effects of the PMT electronics and the size of the detector limit the energy reconstruction ability. In fact, because many of the events are not fully contained at very high energy, part of the Cherenkov cone can miss the PMTs so that part of the charge, that is proportional to the muon energy, is lost. The parent neutrino energy can be inferred from simulation of the $\nu(\bar{\nu}) + N \rightarrow \mu^-(\mu^+)$ interactions. For $E_{\nu,\bar{\nu}} > 10^5$ GeV, the average value of the energy taken by the lepton is ~ 0.75 (63). In most cases, the well reconstructed cascade events develop inside the detector and hence the neutrino energy resolution is largely improved, up to 0.1 - 0.2 in $\log_{10}E_\mu$. Tau neutrinos produce similar events to electron neutrinos up to about 10^6 GeV, because it is not yet demonstrated that NTs have the ability to discriminate between electromagnetic and hadronic showers. However, for $E_\nu \sim 2 \times 10^6$ GeV, once again tau neutrinos deserve a special attention: for such an energy, the tau-lepton range is about 100 m and consequently both the $\nu_\tau N$ interaction and the shower (hadronic or electromagnetic) from the tau decay can be separated (66). These are called double-bang events and are in principle a background-free topology. Nevertheless, the expected event rates are limited by the small energy window in which these events are detectable. As a matter of fact, this topology is limited in energy to the range of a few PeV for the tau track to be long enough, up to about 100 PeV to contain the two cascades in the instrumented volume (the τ range is 1 km at about 200 PeV). The three different neutrino topologies are shown in Fig. 4.

Atmospheric muons and neutrinos constitute a troublesome background for searches of neutrinos produced in astrophysical sources. Moreover, the predictions for such a background are quite uncertain at energies $\gtrsim 1$ TeV. Therefore, background discrimination at NTs requires different techniques depending on the analysis. However, all of these analyses use the fact that neutrinos can cross the entire Earth, though with a shadowing effect that depends on energy and nadir angle. By selecting upgoing muons induced by neutrinos, the residual background of atmospheric muons is largely reduced to those events that are downgoing but are mis-reconstructed as upgoing. For cascade-events background discrimination is instead accomplished through containment cuts, since neutrinos have their vertex in the instrumented region while external tracks are produced mostly by atmospheric muons.

For point source searches, the directional information is the crucial cipher. Being undeflected by intergalactic and galactic magnetic fields, neutrinos preserve directionality from their own sources and tend to cluster around it while the background distribution is random (see Sec. 4.1). The golden channel to point

back to sources is the muon one. This is because the angular resolution is better than 1° , whereas cascade like events have poor resolution of about $10^\circ - 30^\circ$, depending on the medium.

For diffuse flux searches, the energy measurement is determinant. This is because the signal spectrum is expected to be harder than the neutrino background (95) from atmospheric cascades initiated by cosmic rays. When protons and nuclei enter the atmosphere, they collide with the air molecules and produce all kind of secondary particles, which in turn interact or decay or propagate to the ground, depending on their intrinsic properties and energies. Above 1 GeV, the most abundant particles at sea level are neutrinos and muons (50). The properties of these particles, which constitute the main background for astrophysical searches, are described in Sec. 4.2.

3.2 Detectors in operation and decommissioned

The DUMAND and the Baikal collaborations pioneered underwater NT technologies in the deep ocean near Hawaii (67) and in the Siberian Lake Baikal (68), respectively. In November 1987, the DUMAND Collaboration measured the muon vertical intensity at depths ranging between 2 – 4 km, with a prototype line at a depth of 4.8 km about 30 km off-shore of Hawaii (55). The project was canceled in 1995. In 1993 a first configuration of 36 PMTs on 3 strings (NT-36) was installed in Lake Baikal in Siberia at the shallow depth of 1.1 km and 3.6 km off-shore (54). The experiment was later upgraded to larger configurations (NT-72-96-144). In 700 days of effective livetime, 320 million muon events were detected, and the first atmospheric neutrino measured by a neutrino telescope was selected in this sample and reported in 1996. The configuration of the experiment (NT-200) with 192 OMs was put into operation in April 1998. It consists of an umbrella-like structure of 8 (72 m long) strings, with up-looking and down-looking OMs (containing 37-cm diameter PMTs developed for the project, called QUASAR-370). Three external strings at 100 m from the center of NT200, each with 12 pairs of OMs, were added in April 2005 to increase the cascade sensitivity at very high energies (NT200+). The Baikal Collaboration is working towards the construction of a Gigaton-volume detector with about 2100-2500 OMs (arranged over 95-100 strings separated by distances of the order of 80-120 m) grouped in clusters to form independent sub-arrays (69). A prototype string has been taking data since April 2008.

The NESTOR Collaboration began surveys of an area close to the Peloponnese coast at a mean depth of about 4 km in the '90s. They measured the muon flux with a hexagonal prototype floor with 12 up-looking and down-looking PMTs (56), and studied by simulation the possibility to deploy a telescope made of towers with 12 of these hexagonal floors (32 m in diameter) vertically spaced by 20 – 30 m. The Collaboration is operating a deep sea station off-shore of Pylos at a depth exceeding 3.5 km connected to the on shore laboratory by an electro-optical cable.

In 1987 Halzen came out with the idea of “ice-fishing” neutrinos. The Antarctic Muon And Neutrino Detector Array (AMANDA) was located below the surface of the Antarctic ice sheet at the geographic South Pole (70). During 1993 and

1994, in an exploratory phase, the four-string AMANDA – A array was deployed and instrumented with 80 PMTs spaced at 10 m intervals from 810 to 1000 m. (The scattering length at that depth is too short to allow degree level reconstruction.) A deeper array of 10 strings, referred to as AMANDA-B10, was deployed during the austral summers between 1995 and 1997, to depths between 1500 and 2000 m. The instrumented volume of AMANDA-B10 formed a cylinder with diameter 120 m, overlooked by 302 optical modules (Hamamatsu R5912-2 20 cm diameter) (71). During December 1997 and January 2000, the detector was expanded by adding nine outer strings of PMTs. The composite AMANDA-II array of 19 strings and 677 OMs forming two concentric cylinders with larger diameter of 200 m became operative in 2000 and continued up to 2009. The OMs were connected to cables supplying the 8-inch PMT power and transmitting analog signals. Some of the strings used fiber optic cables reducing cross-talk effects, but most used coaxial twisted-pair cables. One of the strings pioneered the digitization technique, with data acquisition for waveform digitization in each module communicating to the surface, designed as a prototype for the IceCube Digital OMs (DOMs) and data transmission.

The IceCube neutrino telescope, currently being deployed near the Amundsen-Scott station, comprises a cubic-kilometer of ultra-clear ice about a mile below the South Pole surface, instrumented with long strings of sensitive photon detectors which record light produced when neutrinos interact in the ice. The deep array is complemented by IceTop, a surface air shower detector consisting of a set of 160 frozen water tanks. With its surface array, IceCube becomes a 3-dimensional air shower array for studies of cosmic rays up to EeV. It is also useful for calibration of the neutrino telescope, and it serves as a partial veto for the downward events at high energy. IceCube strings are placed 124 m apart on a hexagonal grid. Each string is instrumented (between 1.5 to 2.5 km below the surface) with 60 DOMs vertically separated by about 17 m. The DOMs enclose 10-inch Hamamatsu PMTs with quantum efficiency $\sim 20\%$ at around 400 nm. Six additional strings with new high efficiency ($\sim 25 - 30\%$ at 400 nm) PMTs to be deployed in between 7 standard IceCube strings will constitute the Deep Core. It will improve the sensitivity of the detector in the region $\lesssim 1$ TeV, important for dark matter searches and neutrino oscillations. The outer IceCube strings around Deep Core and the upper layers of DOMs will be used as veto-shield against the background of atmospheric muons allowing the identification downgoing neutrino induced muons when the neutrino vertex is in the inner detector. Construction of the observatory will be completed in the austral summer 2010-11. The drilling of strings has been so successful that up to about 20 strings can be installed in a season (from mid-November to mid-February, when airplane flights are possible to and from the South Pole). The basic element of IceCube, the DOM, is made of a glass spherical pressure vessel of 33 cm diameter, containing a 25 cm diameter PMT, a high voltage supply, light emitting diodes for energy and time calibrations, and an electronic motherboard. The motherboard digitizes and time-stamps PMT signals (72). The performance of the first string (deployed in the 2005-6 season), its calibration and test methods, as well as the data acquisition and installation of the detector are described in (73). The layout

of IceCube is shown in Fig. 5.

The completion of the undersea neutrino observatory ANTARES, located at about 2.5 km below the sea surface off-shore Toulon in South France, took several years. Since 1996, the Collaboration had sea campaigns comprising more than 60 line deployments for tests of water transmission, light optical background, bio-deposition and sedimentation (74). The permanent electro-optical cable, of about 40 km, transmitting data and power between the shore station in La Seyne sur Mer and the junction box off shore has been operating since November 2002. Between 2003 and 2005 various prototype lines and a mini-instrumentation line for environmental parameter measurements were deployed (75). In 2006, the first 2 lines of the detector were deployed and 8 additional lines were installed in 2007. On May 2008 ANTARES was completed with a total of 12 lines. Lines were connected initially by a submarine and then by an unmanned Remote Operated Vehicle. The ANTARES observatory comprises the 12 mooring lines, a line specifically dedicated to marine environmental monitoring, a seismometer, and a biocamera for bioluminescence studies. The lines are anchored to sea bed at 2475 m depth and held vertical by buoys. Buoys are freely floating so each line moves under the effect of the sea current, with movements of a few meters for typical values of 5 cm/s. An acoustic positioning system, made of transponders and receivers, gives a real time measurement of the position of the OMs with a precision better than 10 cm, typically every 2 minutes. Tiltmeters and compasses provide their orientation. Seventy-five OMs along each lines between about 2400 and 2000 m are grouped in triplets on storeys. The 3 PMTs (Hamamatsu 10" (76)) look downward at 45° from the vertical to prevent transparency loss due to sedimentation and optimize detection for upgoing tracks. PMTs are housed inside pressure resistant glass spheres made of two halves closed by applying an under-pressure of 200-300 mbar. The set-up, including the PMT, the glass sphere, the silicon gel for optical coupling between the glass and the photocathode, and the mu-metal cage for shielding the Earth magnetic field is referred to as the OM (77). Storeys also include titanium containers housing the front-end electronics, with a pair of ASIC chips per PMT used for signal processing and digitization. This provides the time stamp and the amplitude of the PMT signal. Each of the OMs contains a pulsed LED for calibration of the relative variations of PMT transit time and a system of LED and laser Optical Beacons allows the relative time calibration of different OMs. An internal clock system, which is synchronized by GPS to the Universal Time with a precision of ~ 100 ns, distributes the 20 MHz clock signal from the shore. Time calibrations allow a precision at the level of 0.5 ns ensuring the capability of achieving an angular resolution at the level of 0.3° muons above 10 TeV for point source searches (78). All data above a threshold of about 1/3 of a photoelectron pulse is sent to shore for further online filter. This requires coincidences between PMTs on the same storey rejecting hits not compatible to the propagation of light in water between hit PMTs (79). The ANTARES detector is shown in Fig. 6.

Ice and water are proving to be suitable transmission media with different pros and cons. Photon propagation properties are characterized by a much longer scattering length λ_{scatt} in sea water compared to ice. The effective scattering

length, defined in terms of the average scattering angle of the photons, θ , reads $\lambda_{\text{eff}} = \lambda_{\text{scatt}} / (1 - \langle \cos \theta \rangle)$. In sea water, $\lambda_{\text{eff}} \sim 100 - 200$ m is much larger than in ice due to a more forward peaked angular distribution. On the other hand the absorption length, that determines the distance photons can propagate before being absorbed, is much larger in ice ($\sim 100 - 200$ m) than in water $\sim 50 - 70$ m.

Sea water is a less quiet environment than ice. Additionally, bioluminescence and β -decay of ^{40}K can produce a baseline of optical background in the sea of the order of 30 – 100 kHz and MHz bursts that cause a random dead time for OMs. No current or bioluminescence are present in ice. Once water developed in the drilling process is frozen, the risk of short circuits due to water leakages in the OMs is largely reduced, and PMTs can be switched on. On the other hand, once ice freezes, the components are not recoverable, while entire instrumented lines can be recovered from water for repairs. The average background rate in IceCube PMTs is ~ 280 Hz, mainly dependent on the radioactivity from the OM and PMT materials. The lower optical noise in ice makes IceCube a very sensitive detector for SN collapse searches.⁴

The neutrino effective area, the sensitive area ‘seen’ by neutrinos producing detectable muons when entering the Earth, is a useful parameter to determine event rates and the performance of a detector for different analyses. The expected event rate

$$N_{\mu} = \int \int \int dE_{\nu} d \cos \theta_{\nu} d\phi_{\nu} A_{\nu}^{\text{eff}}(E_{\nu}, \theta_{\nu}, \phi_{\nu}) J_{\nu}(E_{\nu}, \theta_{\nu}, \phi_{\nu}), \quad (22)$$

of a model predicting a neutrino spectrum J_{ν} depends on the neutrino-nucleon cross section $\sigma(E_{\nu})$, the shadowing of the Earth $P_{\text{Earth}}(E_{\nu}, \theta_{\nu})$, the track reconstruction quality cuts, and the selection criteria for background rejection. The shadowing factor depends on column depth, that is the integral of the Earth density profile $\rho(\theta_{\nu}, \ell)$ for a given direction of the neutrino θ_{ν} over the distance in the Earth ℓ : $P_{\text{Earth}}(E_{\nu}, \theta_{\nu}) = e^{-N_A \times \sigma(E_{\nu}) \times \int_{\ell} \rho(\theta_{\nu}, \ell) d\ell}$, where N_A is the Avogadro number. The neutrino effective area is a parameter calculable through simulations and formally given by

$$A_{\nu}^{\text{eff}}(E_{\nu}, \Omega_{\nu}) = V_{\text{eff}}(E_{\nu}, \theta_{\nu}, \phi_{\nu}) \times (\rho N_A) \times \sigma(E_{\nu}) \times P_{\text{Earth}}(E_{\nu}, \theta_{\nu}) \quad (23)$$

where (ρN_A) is the number of nucleons in the target material assumed isoscalar and $V_{\text{eff}}(E_{\nu}, \theta_{\nu}, \phi_{\nu}) = V_{\text{gen}}(E_{\nu}, \theta_{\nu}, \phi_{\nu}) \times N_{\text{sel}}(E_{\nu}, \theta_{\nu}, \phi_{\nu}) / N_{\text{gen}}(E_{\nu}, \theta_{\nu}, \phi_{\nu})$ is the

⁴About 99% of the binding energy of a Type II SN is expected to be released in neutrinos. These SNe originate in the gravitational collapse of massive giant stars, heavier than 8 solar masses, into a neutron star. Current upper limits on the number of supernova explosions in our Galaxy, from scintillator and water Cherenkov detectors, are getting closer to the predicted rates of about 2 per century (85). In the early phase (~ 10 ms), called deleptonization or neutronization, electron neutrinos are emitted in the electron capture process ($e^{-} + p \rightarrow n + \nu_e$) and subsequently (~ 10 s) all neutrino flavors are produced in reactions such as $e^{+} + e^{-} \rightarrow \nu + \bar{\nu}$ in the thermalization phase. The passage of a large flux of MeV-energy neutrinos during a period of seconds will be detected as an excess of single counting rates in all individual optical modules. Each OM will be triggered by positrons from the inverse- β reaction: $\bar{\nu}_e + p \rightarrow e^{+} + n$, where the visible positron energy is given by $E_{\text{vis}} = E_{\bar{\nu}_e} - Q + m_e = E_{\bar{\nu}_e} - 0.789$ MeV (86). IceCube, with 5160 optical modules, can observe the 10 ms pulse as an increased rate over the average background rate (280 Hz) in the PMTs. For example, a SN at a distance of 7.5 kpc would produce a rate of about 10^6 Hz over this time, yielding a 34σ effect. A SN in the Large Magellanic Cloud would produce a 5σ effect.

effective volume of the interactions generated in a volume V_{gen} of the neutrinos that produce detectable muons. The effective volume depends on the energy of the neutrinos that determines how far muons can travel from the vertex (muon range) and accounts for the selection efficiency of an analysis (the efficiency factor $N_{\text{sel}}/N_{\text{gen}}$). The effective areas of the different NTs are compared in Fig. 7.

The point spread function (PSF) is the percentage of muons that are reconstructed inside an angular half-cone width from the neutrino or source direction. It depends strongly on the medium properties and on the reconstruction algorithms. In the final configuration of IceCube, the angular resolution at energies between 10 – 100 TeV will be such that about 50% of the reconstructed muons from the direction of a neutrino point source will be inside an angle of 0.5° . Sea water has longer effective scattering lengths than Antarctic ice hence the resolution in ANTARES or in a future cubic-kilometer detector in the Mediterranean (84) will be of the order of $0.2^\circ - 0.3^\circ$. The PSF of IceCube is shown in Fig. 8.

Cosmic ray experiments, like the Pierre Auger Observatory, provide a complementary technique for ultra-high energy neutrino detection by looking for deeply-developing, large zenith angle ($> 60^\circ$) air showers (87). At these large angles, hadronic air showers have traversed the equivalent of several times the depth of the vertical atmosphere and their electromagnetic component has been extinguished far away from the detector. Only very high energy core-produced muons survive past 2 equivalent vertical atmospheres. Therefore, the shape of a hadronic (background in this case) shower front is very flat and very prompt in time. In contrast, a neutrino shower appears pretty much as a “normal” shower. It is therefore straightforward to distinguish neutrino induced events from background hadronic showers. Moreover, very low ν_τ fluxes could be detected very efficiently by Auger detectors by looking at the interaction in the Earth crust of quasi horizontal ν_τ inducing a horizontal cascade at the detector (88).

4 EXPERIMENTAL RESULTS AND SCIENTIFIC IMPACT

The main goal of neutrino telescopes is detecting astrophysical neutrinos with $E_\nu \gtrsim 100$ GeV. As we noticed in Sec. 3, muons constitute the “golden sample” for neutrino astronomy since the achievable angular resolution is at sub-degree level. At energies $\gtrsim 10$ TeV the limiting angle is mainly due to the transit time spread of the PMTs and to the scattering of light.

While Imaging Atmospheric Cherenkov Telescopes (IACTs) can prove their point spread function on copious sources of gammas, such as the Crab Nebula, no astrophysical high energy neutrino source has proved to exist yet. Hence, the ‘standard candle’ for neutrino telescopes must be an ‘anti-source’, such as the Moon shadow. The Moon disk, with a diameter of about 0.5° , blocks primary cosmic rays hence producing a deficit in the muon flux. IceCube, using 3 months of data of the 40 string configuration, begins to find evidence at 5σ level of this deficit, which is a proof of the absolute timing and pointing capability of the detector (89). A detector with an ice platform on top (like IceCube) is able to test, for a limited solid angle, the angular resolution using events in coincidence

with the extensive air shower array IceTop. Sea detectors, such as ANTARES, can use instead a scintillator array carried by a boat, or the reconstruction of the shape of the close-by continental crust using horizontal muons (90).

4.1 Steady and flaring point-source searches

Searches of point-like sources have various advantages when compared to searches of diffuse fluxes, as in the former one can use the direction, the energy, and eventually the time distributions to reject the background of atmospheric neutrinos. As a matter of fact, the signal is expected to distribute around the source according to the detector PSF, and to have a harder energy spectrum than the background. Flaring sources as well as GRBs are particularly interesting, because if the neutrinos are emitted in coincidence with the gamma flare it is possible to dramatically reduce the background of neutrinos over a short time window. Since the background of the experiment is flat in right ascension (which is directly connected to the hour of the day), many ‘equivalent experiments’ with only background can be reproduced by scrambling the right ascension of events and keeping fixed other information, such as the declination and the energy proxy fixed. This has the advantage that data can be used for estimating the background rather than using simulation, so that resulting significances of the signal and the background are not affected by a possible imperfect understanding of the detector, or similarly the detector medium. Moreover, for searches of flares or GRBs, data outside the short time window can be used to reproduce ‘equivalent experimental’ samples where no signal is present. These techniques are similar to the off-on source techniques applied in photon astronomy, where the background outside the source pixel region is used to evaluate the significance of the observed source. In the many neutrino astronomy point-source searches (91), binned methods that would look for clusters of events on top of the background from specific directions or in the entire sky were applied. The search bin was optimized depending on the expected signal shape (typically assumed to be $\propto E_\nu^{-2}$) but to avoid missing signal events at the border of bins, grids or bins had to be moved, hence, penalizing the search with many trial factors. Many experiments (92) use likelihood methods (93) that can be up to 40% more sensitive depending on the amount of information used. These methods use probability distribution functions that maximize the discrimination between the signal and background. The signal is characterized with respect to the background by the source directional feature and by the harder spectrum expected from astrophysical sources compared to atmospheric neutrinos. For the case of time dependent sources, such as periodical binaries like micro-quasars or flares from blazars, periodicity assumptions or light curves from gamma, X-ray, and optical telescopes can be used.

The IceCube’s 22 string configuration collected 5114 events from the Northern hemisphere in 276 days (80). No signal has been found and upper limits have been set for sources in the Northern hemisphere. For illustrative purposes we note that, for Geminga, the Crab Nebula, Markarian 421, M87, and Cygnus OB2, the upper limits of the 90% CL interval for a flux $\Phi \leq \Phi_{90} \times 10^{-12} \text{TeV}^{-1} \text{cm}^{-2} \text{s}^{-1} (E_\nu/\text{TeV})^{-2}$ are $\Phi_{90} = 9.67, 10.35, 14.35, 7.91, 15.28$, respectively. In addition, a hot spot was found with a post-trial probability of

1.34%. The excess, however, was not confirmed using the 6 month data of the 40 string configuration (that by then encompassed in sensitivity the previous configuration by about a factor of 2) and so the hot-spot has been considered a background fluctuation (83). This 40 string analysis selects upgoing neutrino events from the Northern hemisphere at a rate of about 40 per day. In this region of the sky the experiment is sensitive mainly to events in the 10 – 100 TeV region for a $\propto E_\nu^{-2}$ spectrum. Very recently, by using scrambled background of very high energy atmospheric muons, the IceCube Collaboration extended the field of view for point source searches to the Southern hemisphere. In this area of the sky, the sensitive region, for a spectrum $\propto E_\nu^{-2}$, moves to higher energies (PeV–EeV) (94). As an illustration, the resulting 90%CL upper limits $\Phi \leq \Phi_{90} \times 10^{-9} \text{ GeV}^{-1} \text{ cm}^{-2} \text{ s}^{-1} (E_\nu/\text{GeV})^{-2}$, using 22 strings of IceCube, are $\Phi_{90} = 558.2, 245.0, 27.1$, for Centaurus A, Sagittarius A*, and 3C279 respectively. (The associated energy intervals that contain 90% of the signal are: $\Delta E_\nu/\text{GeV} = 2 \times 10^6 - 8 \times 10^8, 1 \times 10^6 - 9 \times 10^8, 5 \times 10^4 - 1 \times 10^8$.) For the full data sample of 40 strings, the IceCube discovery reach (5σ) for $E_\nu^2 \Phi_{90}$ (averaged over right ascension, and in the declination region between $0^\circ - 90^\circ$) is expected to be between 1 to $5 \times 10^{-11} \text{ cm}^{-2} \text{ s}^{-1}$. This is near to the exclusion flux for 22 strings and about a factor of 3 higher than the exclusion limits for the same configuration. With the 40 strings result, flux limits for galactic sources are beginning to be in the region of interest: $E_\nu^2 \Phi \sim 10^{-12} - 10^{-11} \text{ TeV cm}^{-2} \text{ s}^{-1}$ (see Sec. 2). Actually, according to estimates based on gamma-ray observations it would be possible to achieve 5σ significance for Milagro Pevatrons, with ~ 10 yr of IceCube data collection (6). The 40 string sky-map is shown in Fig. 9.

4.2 Atmospheric muons and neutrinos

Atmospheric muons and neutrinos detected by NTs above some tens of GeVs are produced in cosmic ray induced showers and come mainly from pions and kaons. At lower energies ($\lesssim 10 \text{ GeV}$) muon and electron neutrinos are also generated by muon decays. They were extensively studied in the past two decades because of the so called “atmospheric neutrino problem,” a deficit of muon induced neutrino events that was explained by muon neutrino oscillations into tau neutrinos [for a review see, e.g., (95, 96)]. At energies above 100 GeV, where NTs operate, atmospheric neutrino oscillation studies are not a primary target. Nonetheless, although DeepCore and ANTARES photocathode coverage are modest, they will collect a very large statistics of atmospheric neutrinos opening the possibility of observing neutrino oscillations. The main interests for NTs to measure atmospheric neutrinos are (i) calibration of the detector, demonstrating their ability to discriminate neutrino events from the huge background of atmospheric muons; (ii) understanding of hadronic interactions in the forward region, at energies not yet accessible by colliders; and (iii) study of new physics scenarios.

The dominant production channels of atmospheric and muon neutrinos detected in NTs are the decay chains of mesons created in hadronic cascades. The pion decay chain ($\pi^+ \rightarrow \mu^+ \nu_\mu \rightarrow e^+ \nu_e \nu_\mu \bar{\nu}_\mu$ and the conjugate process) dominates the atmospheric neutrino production at $\sim \text{GeV}$ energies. At energies of some GeVs, the muon decay length begins to be comparable to the atmospheric

altitude where most muons and neutrinos are produced (10 – 20 km). Hence, depending on the incoming zenith angle, muons may stop decaying. At energies of about 100 GeV kaon decay becomes increasingly important with respect to pion decay. In this energy range, the atmospheric neutrino spectrum can be parametrized as (26)

$$\frac{dN_{\nu_\mu}}{d\ln E_\nu} = A_{\text{tot}} E_\nu^\alpha \left[\frac{A_\nu}{1 + B_p E_\nu (\cos \theta)^* / \epsilon_\pi} + 0.635 \times \frac{B_\nu}{1 + B_k E_\nu (\cos \theta)^* / \epsilon_k} \right] \quad (24)$$

where 0.635 is the branching ratio of K^\pm decays; $\epsilon_\pi = 115$ GeV and $\epsilon_K = 850$ GeV are the critical energies respectively for pion and kaon decay, $\alpha \sim 1.7$ is the spectral index of the primary spectrum, A_{tot} ; A_ν and B_ν are normalization constants; and B_p and B_k are constant terms with energy. The term $(\cos \theta)^*$ is equal to $\cos \theta$ for zenith angles such that $\cos \theta \lesssim 0.3$, and for horizontal directions ($\cos \theta \gtrsim 0.3$) it has a larger value that accounts for the curvature of the Earth. The $1/(E_\nu \cos \theta)$ dependence, is characteristic of atmospheric processes where there is competition between interaction and decay, since the decay probability increases with respect to the interaction one for longer horizontal paths in the atmosphere. The muon flux in this energy region has a similar dependence with the important difference on the energy fraction taken by muons in two body pion and kaon decays. We remind the reader that, on average, in pion decay the neutrino takes a quarter of the energy of the pion while the muon takes the rest. This implies that above ~ 1 TeV, muon production is dominated by pion decay and neutrino production by kaon decay (about 85% of the muons are produced via pion decay, whereas only 25% of neutrinos come from the decay of charged pions). The electron neutrino formula is more complicated, with two similar terms due to K^\pm and K_L decays from which ν_e are produced directly, and a term due to muon decay into electron neutrinos determined by π^\pm , K^\pm and K_L decays. In this energy window, the flavor ratios are $w_e : w_\mu : w_\tau \approx 1/20 : 19/20 : 0$ (97) and the energy spectra are a function of the zenith angle of the atmospheric cascades. As already observed, mesons in inclined showers spend more time in rarefied atmosphere where they are more likely to decay rather than interact. For this reason the spectra of highly inclined neutrinos are harder than those of almost vertical neutrinos and resemble their primary spectrum. Above about 10^5 GeV, kaons are also significantly attenuated before decaying and the “prompt” component, arising mainly from very short-live charmed mesons (D^\pm , D^0 , D_s and Λ_c) dominates the spectrum (18). Such a “prompt” neutrino flux is isotropic with flavor ratios $12/25 : 12/25 : 1/25$. Since prompt neutrinos have a hard spectrum resembling the primary one (below the knee the differential cosmic ray spectrum goes as $\sim E^{-2.7}$), they are a persisting background for astrophysical neutrinos that follow a power law $\sim E_\nu^{-2}$.

Various Monte Carlo high precision calculations have been developed for studying the atmospheric neutrino oscillations (58,95,98). For energies below 10 GeV, high precision needs to account for the angle of secondaries with respect to primaries (99), the solar modulation effects, and the Earth geomagnetic field deflections. At higher energies these effects become negligible and one dimensional calculations that neglect the angle of secondaries respect to primaries are suit-

able. Uncertainties in atmospheric neutrino fluxes are of the order of 15% in the region of ~ 10 GeV, rising to about 20-30% at ~ 100 GeV–1 TeV (100). These are mainly due to the rather poor knowledge of the primary cosmic ray flux and the hadronic interaction models. A precise estimate in the prompt region is not possible since charm production in the atmosphere is not well constrained by collider measurements (101). The various calculations differ by up to 2 orders of magnitude (18). Some of them are shown in Fig. 3 (59–61). The experiments LHCf and TOTEM, dedicated to measure particles emitted in the very forward region (102), will improve our understanding of hadronic models at laboratory energies of about 10^{17} eV.

A cubic-km NT measures of the order of kHz muon events, the so-called “second calibration beam.” With such a high statistics, high precision verifications become possible; e.g., how well the detector details and the effects of the light propagation in the radiator are simulated. Nonetheless, hadronic interaction models used in the atmospheric shower simulations are affected by theoretical uncertainties, not only experimental ones. Some of these models are similar to those used to simulate atmospheric neutrinos. This represents a drawback, because the two calibration beams should be used to understand the ‘same’ detector independently of theoretical uncertainties. Another complication that affects shower models is the difficulty of investigating separately errors coming from imperfect knowledge of high energy primary cosmic ray composition and hadronic model, and from the fact that simulations do not account for the seasonal variation of the atmosphere. These simulations are very time consuming since rates of events are very high and high energy showers develop many particles in the atmosphere. Hadronic interaction models that foresee a larger K^+ production (such as SIBYLL 2.1) show better agreement than others (e.g. QGSJET II) in the high $x = E_{\text{secondary}}/E_{\text{primary}}$ region (103). The preference for such hadronic models is also indicated by the muon ratio measurement of MINOS (104) that shows a rise between 0.3 – 1 TeV consistent with an increasing contribution to the muon charge ratio from kaons.

A neutrino telescope’s high statistics measurement of the atmospheric neutrino flux above about 100 GeV is an important benchmark for all these calculations. A fit of the atmospheric muon neutrino flux [see Eq. (24)] was recently performed with AMANDA-II data to determine variations with respect to existing models (105). The allowed region in the parameter space normalization vs spectral index was derived relative to the Bartol flux (98), using the angular distribution and an energy proxy for 5511 neutrino events collected in 1387 d. The best fit point indicates that, at 640 GeV, the data prefer a higher normalization by about 10% and a slightly harder spectrum by about 0.056. Using a sample of 4492 upgoing neutrino induced muon events collected in 275.5 days, with a contamination of 5% from misreconstructed atmospheric muons, the IceCube Collaboration unfolded the atmospheric neutrino spectrum for the 22 string configuration (57). This spans a wider energy range up to PeV energies and is compared to some conventional (from π and K decays) and prompt neutrino models in Fig. 3. Systematic errors are so large at $E_\nu > 10$ TeV that it is not yet possible to disentangle an eventual contribution from prompt neutrinos (originating in the decay

of charmed mesons and baryons) from an astrophysical component (60).

Neutrino telescopes can collect a huge statistics of muons, of the order of billions. Thus, they are sensitive to anisotropies of amplitudes $< 10^{-3}$. For example, in Fig. 10 we show the map in equatorial coordinates of about 5 billion atmospheric muons detected with the 22 strings of IceCube. These muons are produced by cosmic rays with a median energy of 14 TeV and have a median angular resolution of 3° , and show an anisotropy in their arrival direction of amplitude $(6.4 \pm 0.2) \times 10^{-4}$. The observed anisotropy persists with high statistical significance, to energy in excess of 100 TeV with a smaller but measurable amplitude. This observation is not compatible with the Compton-Getting effect (109), which produces an energy-independent dipole anisotropy in the arrival direction of cosmic rays due to the relative motion of the solar system with respect to the rest frame of galactic cosmic rays (GCRs). This explanation was already excluded by Tibet Array (107) that in the absence of an anisotropy at 300 TeV concluded that GCRs co-rotate with the Galaxy. Other experiments observed anisotropies in the Northern hemisphere at the scale of $10^\circ - 30^\circ$ (108). Particularly Milagro applied a cut that discriminates hadrons with respect to gammas. The observed anisotropy with IceCube in the opposite hemisphere persists at energies > 100 TeV, and hence makes it difficult to explain it as an effect of the heliosphere or the heliospheric tail. Interestingly, it has been speculated that the effect may be due to the propagation of cosmic rays produced by nearby (~ 100 pc) SNRs and pulsars (110). It is noteworthy the presence of Geminga between the anisotropy regions in the Northern hemisphere. In the Southern hemisphere, the Vela pulsar is located near the highest intensity regions observed by IceCube. Of course such regions are so broad that we can only speculate about responsible local sources in the absence of a more precise calculation, including the intensity of galactic magnetic fields. This in turn could be correlated to observations at lower energies of an excess in the positrons to electron fraction with respect to secondary production models (111) that have also been interpreted as propagation of cosmic rays from local sources such as SNRs and pulsars (112). It has also been speculated that the sites of the acceleration of cosmic rays may not be isolated, but also involve superbubbles (overlapping SNRs) (113).

4.3 Searches for diffuse cosmic neutrino fluxes

Diffuse fluxes from extra-galactic sources are more promising compared to single source fluxes because of the larger event rates, with a signal that may extend up to the highest energies where some of the extra-galactic sources (e.g., as AGNs and GRBs) can contribute. Nonetheless, these searches have to rely more on simulations than point source searches and hence are subject to larger systematic errors. The basic concept is that because of the harder spectrum the astrophysical signal should show up at high energies above the atmospheric neutrino background. However, the theoretical uncertainties on high energy atmospheric neutrino fluxes (see Sec. 4.2) and the experimental errors in the high energy region where the statistics is low, limit the sensitivity and reliability of this search. For large statistics, the uncertainty in the prompt neutrino flux can be mitigated by triggering on tau neutrinos, which have the double bang characteristic signa-

ture in the PeV energy range, see Fig. 4. Specifically, the detection of a double bang event would confirm neutrino oscillations and at the same time establish the discovery of high energy cosmic neutrinos; this is because tau neutrino production in the atmosphere is negligible. Figures 11 (experiments measuring 1 flavor) and 12 (experiments measuring all neutrino flavors) present a collection of experimental limits compared to representative models for classes of sources, such as AGNs, GRBs, and cosmogenic neutrinos. These upper limits can in turn be used to constrain the origin and nature of ultra-high energy cosmic rays. It is this that we now turn to study.

4.4 Cosmic ray proton fraction

Consider the working hypothesis introduced in Sec. 2 for optically thin sources, i.e., the relative number and energy of the neutrinos and neutrons depend only on kinematics, which implies approximate equipartition of the decaying pion's energy between the neutrinos and the electron, and the relative radiation density in the source. On average, each interaction will produce η neutrinos per neutron with relative energy ϵ per neutrino, i.e. $\eta = \langle N_\nu \rangle / \langle N_n \rangle$ and $\epsilon = \langle E_\nu \rangle / \langle E_n \rangle$. The neutrino emissivity of flavor i is then given by

$$\frac{\Delta E_{\nu_i}}{N_{\nu_i}} \mathcal{L}_{\nu_i}(z, E_{\nu_i}) = \frac{\Delta E_n}{N_n} \mathcal{L}_n(z, E_n). \quad (25)$$

Assuming flavor universality as well as $\epsilon \simeq E_\nu / E_n \simeq \Delta E_\nu / \Delta E_n$ and $\eta \simeq N_{\text{all } \nu} / N_n$ one arrives at the neutrino source luminosity (per co-moving volume)

$$\mathcal{L}_{\text{all } \nu}(z, E_\nu) \simeq \frac{\eta}{\epsilon} \mathcal{L}_n(z, E_\nu / \epsilon). \quad (26)$$

For the (hypothetical) source where pion production proceeds exclusively via resonant $p\gamma \rightarrow \Delta^+$ scattering, the neutrino multiplicity and the relative energy are fixed: $\eta = 3$ and $\epsilon = 0.07$. Note, that the relation (26) derived for optically thin sources can be regarded as a *lower* limit on the neutrino luminosity as long as energy-loss processes in the source are negligible (122). Therefore, this conservative expectation can be translated into an *upper* limit on the extra-galactic proton fraction in ultra-high energy cosmic rays, exploiting, e.g., the experimental upper limit on the diffuse neutrino flux from IceCube or the preliminary AMANDA data (119).

For this procedure one introduces test functions of the neutron source luminosity of the form $\mathcal{L}_n^{\text{test}}(0, E) = \mathcal{L}_0 (E/E_{\text{max}})^{-1} \exp(-E/E_{\text{max}})$, with an exponential energy cut-off E_{max} that varies between 10^8 GeV and 10^{12} GeV with a logarithmic step-size of $\Delta \log_{10} E = 0.25$ (122). The source function per unit redshift is given in Eq. (19). The source luminosity per co-moving volume is assumed to follow that of the star formation rate (SFR): $\mathcal{H}_{\text{SFR}}(z) = (1+z)^{3.4}$, for $z < 1$, $\mathcal{H}_{\text{SFR}}(z) = N_1(1+z)^{-0.3}$, for $1 < z < 4$, and $\mathcal{H}_{\text{SFR}}(z) = N_1 N_4 (1+z)^{-3.5}$, for $z > 4$, with appropriate normalization factors, $N_1 = 2^{3.7}$ and $N_4 = 5^{3.2}$ (123). Each neutron test luminosity is related to a neutrino luminosity by the ratio (26). After propagation, the accumulated contribution of extra-galactic and cosmogenic neutrinos is normalized to the neutrino limit. The results are shown in Fig. 13.

The AMANDA preliminary limit on the diffuse neutrino flux (119) severely constrains the extragalactic proton contribution in cosmic rays at energies below 10^9 GeV. Following the same line of thought, one can verify that if the evolution of cosmic ray sources follows that of active galactic nuclei (124), the upper limit on the diffuse flux of tau neutrinos from the Pierre Auger Observatory (117) marginally constrains the proton fraction at the end of the spectrum (125).

4.5 Dark matter searches

Over the past few years, a flood of high-quality data (126) from the Supernova Cosmology Project, the Supernova Search Team, the Wilkinson Microwave Anisotropy Probe (WMAP), the Two Degree Field Galaxy Redshift Survey (2dFGRS), and the Sloan Digital Sky Survey (SDSS) pin down cosmological parameters to percent level precision, establishing a new paradigm of cosmology. A surprisingly good fit to the data is provided by a simple geometrically flat Friedman-Robertson-Walker universe, in which 30% of the energy density is in the form of non-relativistic matter ($\Omega_m = 0.30 \pm 0.04$) and 70% in the form of a new, unknown dark energy component with strongly negative pressure ($\Omega_\Lambda = 0.70 \pm 0.04$). The matter budget has only 3 free parameters: the Hubble parameter $h = 0.70_{-0.03}^{+0.04}$, the matter density $\Omega_m h^2 = 0.138 \pm 0.012$, and the density in baryons, $\Omega_b h^2 = 0.0230_{-0.0012}^{+0.0013}$.⁵ This implies that the structure of the universe is dictated by the physics of as-yet-undiscovered cold dark matter ($\Omega_{\text{CDM}} h^2 = 0.115 \pm 0.012$) and the galaxies we see today are the remnants of relatively small overdensities in the nearly uniform distribution of matter in the very early universe.

The simplest model for cold dark matter consists of WIMPs - weakly interacting massive particles (128). The most popular CDM candidates are (i) the lightest supersymmetric particle (such as the well motivated neutralino χ) that is stabilized in R -parity conserving models of supersymmetry (SUSY) (129) and (ii) the lightest Kaluza-Klein state appearing in models of universal extra dimensions (130). Generic WIMPs were once in thermal equilibrium, but decoupled while strongly non-relativistic. The relic abundance of SUSY WIMPs can be found by integrating the Boltzman equation (131),

$$\frac{dn}{dt} + 3Hn = -\langle\sigma v\rangle(n^2 - n_{\text{eq}}^2), \quad (27)$$

where n is the present number density of SUSY WIMPs, H is the expansion rate of the universe at temperature T , $n_{\text{eq}} = g(m_\chi T/2\pi)^{3/2} e^{-m_\chi/T}$ is the equilibrium number density, g is the number of internal degrees of freedom of the WIMP, $\langle\sigma v\rangle$ is the thermally averaged annihilation cross section, and m_χ is the neutralino mass. Note that in the very early universe, when $n \simeq n_{\text{eq}}$, the right hand side of Eq. (27) is small and the evolution of the density is dominated by Hubble expansion. As the temperature falls below m_χ , however, the equilibrium number density becomes suppressed and the annihilation rate increases, rapidly reducing the number density. Finally, when the number density falls enough, the rate of depletion due to expansion becomes greater than the annihilation rate, $H \geq$

⁵The latter is consistent with the estimate from Big Bang nucleosynthesis, based on measurements of deuterium in high redshift absorption systems, $\Omega_b h^2 = 0.020 \pm 0.002$ (127).

$n\langle\sigma v\rangle$, and the neutralinos *freeze out* of thermal equilibrium. The freeze-out temperature T_f depends logarithmically upon $\langle\sigma v\rangle$, but for models with TeV scale SUSY breaking, one finds that $T_f/m_\chi \sim 0.05$. SUSY WIMPs are, by far, the favored candidate for CDM, because for masses of order 100 GeV to 10 TeV a present density of $\Omega_\chi h^2 \sim 0.1$, comes out fairly natural (132).

Many approaches have been developed to attempt to detect dark matter. Such endeavors include direct detection experiments which hope to observe the scattering of dark matter particles with the target material of the detector (133) and indirect detection experiments which are designed to search for the products of WIMP annihilation into gamma-rays, anti-matter, and neutrinos (134).

The annihilation of WIMPs into photons typically proceeds through a complex set of processes, and the final spectrum actually contains a detailed imprint of WIMP annihilation that can, in principle, reveal features such as the WIMP spin and/or other particles in the dark sector (135). On the one hand, tree-level annihilation of WIMPs into quarks or leptons (or heavier states which decay into them) yields a continuum of photon energies, with an upper cutoff at approximately the WIMP mass. On the other hand, loop-level annihilation into a photon and X results in a line at energy $E_\gamma = m_\chi[1 - M_X^2/(4m_\chi^2)]$, where M_X is the X -boson in the final state (in SUSY models, X is either another photon or a Z). The line emission typically has smaller magnitude than continuum emission, but it provides a clean signal that helps discriminate against backgrounds. The differential flux of photons arising from CDM annihilation observed in a given direction making an angle ψ with the direction of the galactic center (GC) is given by (135)

$$\phi^\gamma(\psi, E_\gamma) = \int \bar{J} \frac{1}{2} \frac{D_\odot}{4\pi} \frac{\rho_\odot^2}{m_\chi^2} \sum_f \langle\sigma v\rangle_f \frac{dN_f}{dE_\gamma} d\Omega, \quad (28)$$

where $\bar{J} = (1/\Delta\Omega) \int_{\Delta\Omega} J(\psi) d\Omega$ denotes the average of J over the solid angle $\Delta\Omega$ (corresponding to the angular resolution of the instrument) normalized to the local density: $J(\psi) = (D_\odot \rho_\odot^2)^{-1} \int_{\ell=0}^{\infty} \rho^2[r(\ell, \psi)] d\ell$; the coordinate ℓ runs along the line of sight, which in turn makes an angle ψ with respect to the direction of the GC (i.e., $r^2 = \ell^2 + D_\odot^2 - 2\ell D_\odot \cos\psi$); the subindex f denotes the annihilation channels with one or more photons in the final state and dN_f/dE_γ is the (normalized) photon spectrum per annihilation; and $\rho(\vec{x})$, $\rho_\odot = 0.3 \text{ GeV/cm}^3$, and $D_\odot \simeq 8.5 \text{ kpc}$ respectively denote the CDM density at a generic location \vec{x} with respect to the GC, its value at the solar system location, and the distance of the Sun from the GC. Indeed, the GC has long been considered to be among the most promising targets for detection of CDM annihilation, particularly if the halo profile of the Milky Way is cusped in its inner volume (136). This has been complicated, however, because H.E.S.S. observations disfavored CDM emission from the GC, and revealed instead a VHE source (HESS J1745-290) (137). To discover CDM photon emission the contribution of the many point sources near GC (138) needs to be subtracted. IACTs or satellite and balloon-borne experiments also look for gammas from high CDM density regions relatively close to the Earth ($\gtrsim 100 \text{ kpc}$) such as dwarf spheroidal satellite galaxies of the Milky Way, clusters of galaxies, and intermediate mass black holes (85).

Neutrino telescopes indirectly search for the presence of dark matter by taking advantage of the Sun's ability to capture large numbers of WIMPs over time. Over billions of years, a sufficiently large number of WIMPs can accumulate in the Sun's core to allow for their efficient annihilation. Such annihilations produce a wide range of particles, most of which are quickly absorbed into the solar medium. Neutrinos, on the other hand, may escape the Sun and be detected in experiments on the Earth. Specifically, the time evolution of the WIMP population in the Sun is controlled by

$$\dot{N} = C_{\odot} - A_{\odot}N^2, \quad (29)$$

where

$$C_{\odot} \approx 3 \times 10^{18} \text{ s}^{-1} \left(\frac{\rho_{\text{local}}}{0.3 \text{ GeV/cm}^3} \right) \left(\frac{270 \text{ km/s}}{\bar{v}_{\text{local}}} \right)^3 \left(\frac{\sigma_{\text{eff}}}{10^{-6} \text{ pb}} \right) \left(\frac{1 \text{ TeV}}{m_{\chi}} \right)^2 \quad (30)$$

is the Sun's rate of capture (139), ρ_{local} is the local dark matter density, \bar{v}_{local} is the local rms velocity of halo dark matter particles, $A_{\odot} = \langle \sigma v \rangle / V_{\text{eff}}$, $V_{\text{eff}} = 1.8 \times 10^{26} (\text{TeV}/m_{\chi})^{3/2} \text{ cm}^3$ is the effective volume of the core Sun determined by matching the core temperature with the gravitational potential energy of a single WIMP at the core radius (140), and A_{\odot} is related to the annihilation rate by

$$\Gamma = \frac{1}{2} A_{\odot} N^2. \quad (31)$$

The rate at which WIMPs are captured in the Sun depends on the nature of the interaction the WIMP undergoes with nucleons in the Sun. These elastic scattering processes are often broken into two classifications: *spin dependent* interactions in which cross sections, σ_{SD} , increase with the spin of the target nuclei, and *spin independent* interactions in which cross sections, σ_{SI} , increase as the square of the total number of nucleons in the target. Thus, the effective WIMP-on-nucleus (hydrogen and helium) elastic scattering cross section has two contributions: $\sigma_{\text{eff}} = \sigma_{\text{SD}} + \sigma_{\text{ID}}$. The present WIMP annihilation rate is found by solving Eq. (29) for the annihilation rate at a given time

$$\Gamma = \frac{1}{2} C_{\odot} \tanh^2 \left(\frac{t}{\tau_{\text{eq}}} \right), \quad (32)$$

where $\tau_{\text{eq}} = 1/\sqrt{C_{\odot} A_{\odot}}$ is the time scale required to reach equilibrium between capture and annihilation. When τ_{eq} becomes comparable or larger than the age of the solar system ($t_{\odot} \simeq 4.5$ billion years), the system has not yet reached equilibrium and the annihilation rate is strongly suppressed $\Gamma \approx \frac{1}{2} C_{\odot} (\sqrt{C_{\odot} A_{\odot}} t_{\odot})^2$, whereas when $(C_{\odot} A_{\odot}) t_{\odot} \gg 1$ the annihilation rate is saturated at $\Gamma = \frac{1}{2} C_{\odot}$.

As they annihilate, WIMPs can generate neutrinos through a wide range of channels. Annihilations to heavy quarks, tau leptons, gauge bosons and Higgs bosons can all generate neutrinos in the subsequent decay (22). The total flux of neutrinos emitted by the Sun due to WIMP annihilation is then

$$\left. \frac{dF_{\odot}^{\nu\mu}}{dE_{\nu}} \right|_{\text{source}} = C_{\odot} F_{\text{Eq}} \sum_j \left(\frac{dN_{\nu\mu}}{dE_{\nu}} \right)_j e^{-E_{\nu}/150 \text{ GeV}}, \quad (33)$$

where F_{Eq} is the non-equilibrium suppression factor (≈ 1 for capture-annihilation equilibrium) and $(dN_{\nu_\mu}/dE_\nu)_j$ is the ν_μ flux produced by the j decay channel per WIMP annihilation. Note that neutrinos produced near the center of the Sun interact with the solar medium, yielding a depletion of the emission spectrum by a factor $\sim e^{-E_\nu/150 \text{ GeV}}$ (22). Finally, the ν_μ flux reaching the Earth is,

$$\phi_\odot^{\nu_\mu} = \frac{1}{4\pi d^2} \left. \frac{dF_\odot^{\nu_\mu}}{dE_\nu} \right|_{\text{source}}, \quad (34)$$

where $d \approx 1.5 \times 10^8$ km is the Earth-Sun distance. All in all, the prospects for neutrino-detection-experiments detecting dark matter critically depend on the capture rate of WIMPs in the Sun, which in turn depends on the elastic scattering cross section of these particles.

While gamma-ray experiments set limits on $\langle\sigma v\rangle$ or on the gamma-ray flux, neutrino telescopes measure the muon induced flux by neutrinos and hence constrain this flux as a function of m_χ . A collection of various limits on the muon flux is shown in Fig. 14. The conversion from muon flux to cross section limits is not model independent; in Fig. 15 it was done using DarkSUSY (150). Equilibrium is assumed between capture and annihilation rates in the Sun, so that the annihilation rate is proportional to the spin-dependent and independent cross sections. A limit on σ_{SD} is found by setting to zero the spin-independent cross section. This procedure is indispensable to show complementarity between searches and to combine results from different techniques. As an illustration, in Fig. 15 we compare the limits on σ_{SD} with those obtained from direct detection experiments including CDMS (141), COUPP and KIMS (149).

The described indirect searches for CDM are complementary approaches to the direct searches and the possible direct production at LHC. Though indirect detection channels are subject to large astrophysical uncertainties, they explore different regions of the parameter space and a very wide range of candidate particle masses.

5 CONCLUSIONS AND FUTURE PROSPECTS

The hunt for neutrinos has just begun with suitable size detectors for the expected small event rates. Given their dimensions these experiments are very challenging to build. IceCube, the first cubic-kilometer detector, is expected to be completed on schedule in 2011. If the predictions from the measured gamma-ray fluxes are indeed correct, then the first detection of sources, such as the ‘‘Milagro Pevatrons’’ with hard spectra up to a few tens of TeV, may become possible after a few years of data taking. Neutrino telescopes may broaden our reach to the unknown like many other astronomical instruments which have discovered unexpected signals from the Universe; NTs can access sources that are opaque in photons. The Mediterranean community is operating ANTARES, the first complete underwater detector, at the scale of the IceCube’s precursor AMANDA-II. Other R&D programs are ongoing to build a cubic-km detector in the Mediterranean sensitive to the GC. In Italy, a ~ 100 km electro-optical cable has been installed off-shore Capo Passero (at about 3.5 km below sea surface) by the NEMO Col-

laboration, in July 2007. A prototype tower of the proposed cubic-km array will be connected in the near future. ANTARES, NEMO and NESTOR joined their efforts forming the Consortium KM3NeT to design the cubic-km detector in the Mediterranean. High quantum efficiency PMTs are being studied for this cubic-km detector in the Mediterranean. Most of the proposals aim at increasing the photocathode area per OM and the isotropy of light detection, minimizing the transit time spread, maximizing the collection efficiency and the peak to valley ratio for a single photoelectron signal (connected to the capability of counting photoelectrons in one event), and minimizing costs and power consumption.

Building a detector a factor of 10 more sensitive than IceCube does not seem to be an easy task to achieve, neither in the ice nor in the sea. A new detector in the sea, with similar cost to IceCube, could not achieve such a goal with the current technology, despite the fact that in the sea the angular resolution for point source searches can be better by a factor of 2-3 compared to IceCube. It is also hard to obtain a uniform increment in area at all energies, while avoiding cost divergence. A significant increase in the area at very large energies implies larger separations between instrumented lines. Hence, this penalizes the 1–100 TeV region, that is an important region for galactic sources.

Projects are underway to build detectors of the order of 100 times IceCube using techniques that exploit the advantage of attenuation lengths about a factor of 10 greater than the optical one in the same medium. Particularly interesting is the radio technique in ice. The acoustic technique in sea water or ice seems also encouraging. None of these techniques, however, is background free. Moreover, they have the disadvantage of higher energy thresholds compared to the NTs discussed in this review. Clearly the higher thresholds reduces the degree of overlap with the optical technique, preventing effective cross-calibrations that would help the understanding of the background. Moreover, thresholds of the order of 10^{18} eV are suitable for extragalactic neutrinos but not for galactic sources. Detectors combining the radio and acoustic techniques are also desirable. However, for cross-calibrations, the radio technique seems currently more promising due to the low cost of antennas, the lower power consumption than acoustic devices, and the larger attenuation length in the ice.

In summary, after 20 years of careful work by many research groups around the world we are in possession of a tantalizing body of data, more than sufficient to stimulate our curiosity but not yet sufficient to pin down high energy neutrino sources. The upcoming high quality observations from the “giant-aperture” neutrino telescopes under construction will generate a data sample of unprecedented size, ushering us to a golden age of neutrino astronomy.

Acknowledgments

We are grateful to Markus Ahlers, Francis Halzen, Luciano Moscoso, Paolo Desiati, Ellen Zweibel, Christian Spiering, Tom Gaisser, Todor Stanev, Tom Weiler, Francesco Arneodo, Haim Goldberg, Subir Sarkar, Diego Torres, Evelyn Malkus for comments and discussions. L.A.A. is supported by the U.S. National Science Foundation Grant No PHY-0757598, and the UWM Research Growth Initiative.

T.M. is supported by U.S. National Science Foundation-Office of Polar Program, U.S. National Science Foundation-Physics Division, and University of Wisconsin Alumni Research Foundation and by INFN, Sezione di Bari, Italy.

LITERATURE CITED

1. Reines F, *Ann. Rev. Nucl. Part. Sci.* **10**:1 (1960);
Greisen K, *Ann. Rev. Nucl. Part. Sci.* **10**:63 (1960);
Gaisser TK, Halzen F, Stanev T, *Phys. Rept.* **258**:173 (1995) [Erratum-ibid. **271**:355 (1996)] [arXiv:hep-ph/9410384];
Learned JG, Mannheim K, *Ann. Rev. Nucl. Part. Sci.* **50**:679 (2000);
Halzen F, Hooper D, *Rept. Prog. Phys.* **65**:1025 (2002) [arXiv:astro-ph/0204527];
Lipari P, *Nucl. Instrum. Meth. A* **567**:405 (2006) [arXiv:astro-ph/0605535].
2. Bahcall JN, Fowler WA, Iben I, Sears RL, *Astrophys. J.* **137**:344 (1963).
3. Cleveland BT *et al.*, *Astrophys. J.* **496**:505 (1998);
Hirata KS *et al.* [KAMIOKANDE-II Collaboration], *Phys. Rev. Lett.* **63**:16 (1989);
Fukuda Y *et al.* [Super-Kamiokande Collaboration], *Phys. Rev. Lett.* **81**: 1158 (1998) [Erratum-ibid. **81**, 4279 (1998)] [arXiv:hep-ex/9805021];
Ahmad QR *et al.* [SNO Collaboration], *Phys. Rev. Lett.* **89**:011301 (2002) [arXiv:nucl-ex/0204008].
4. Hirata K *et al.* [KAMIOKANDE-II Collaboration], *Phys. Rev. Lett.* **58**:1490 (1987);
Bionta RM *et al.*, *Phys. Rev. Lett.* **58**:1494 (1987).
5. Erlykin AD, Wolfendale AW, *J. Phys. G* **31**:1475 (2005) [arXiv:astro-ph/0510016];
Alvarez-Muniz J, Halzen F, *Astrophys. J.* **576**:L33 (2002) [arXiv:astro-ph/0205408];
Morlino G, Blasi P, and Amato E, *Astropart. Phys.* **31**:376 (2009) [arXiv:0903.4565 [astro-ph.HE]];
Villante FL and Vissani F, *Phys. Rev. D* **78**: 103007 (2008) [arXiv:0807.4151 [astro-ph]].
6. Anchordoqui L, Halzen F, Montaruli T, O’Murchadha A, *Phys. Rev. D* **76**:067301 (2007) [Erratum-ibid. *D* **77**:069906 (2008)] [arXiv:astro-ph/0612699];
Beacom JF, Kistler MD, *Phys. Rev. D* **75**:083001 (2007) [arXiv:astro-ph/0701751];
Halzen F, O Murchadha A, *Phys. Rev. D* **76**:123003 (2007) [arXiv:0705.1723 [astro-ph]];
Halzen F, Kappes A, O’Murchadha A, *Phys. Rev. D* **78**:063004 (2008) [arXiv:0803.0314 [astro-ph]].
7. Levinson A, Waxman E, *Phys. Rev. Lett.* **87**:171101 (2001) [arXiv:hep-ph/0106102];
Distefano C, Guetta D, Waxman E, Levinson A, *Astrophys. J.* **575**:378 (2002) [arXiv:astro-ph/0202200].
8. Aharonian FA, L. A. Anchordoqui LA, Khangulyan D, Montaruli T, *J. Phys. Conf. Ser.* **39**:408 (2006) [arXiv:astro-ph/0508658];
Torres DF, Halzen F, *Astropart. Phys.* **27**:500 (2007) [arXiv:astro-

- ph/0607368].
9. Amato E, Guetta D, Blasi P, *Astron. Astrophys.* **402**:827 (2003) [arXiv:astro-ph/0302121];
Bednarek W, *Mon. Not. Roy. Astron. Soc.* **345**:847 (2003) [arXiv:astro-ph/0307216].
 10. Bednarek W, Burgio GF, Montaruli T, *New Astron. Rev.* **49**:1 (2005) [arXiv:astro-ph/0404534];
Becker JK, *Phys. Rept.* **458**:173 (2008) [arXiv:0710.1557 [astro-ph]].
 11. Kistler MD, Beacom JF, *Phys. Rev. D* **74**:063007 (2006) [arXiv:astro-ph/0607082];
Kappes A, Hinton J, Stegmann C, Aharonian FA, *Astrophys. J.* **656**:870 (2007) [Erratum-ibid. **661**:1348 (2007)] [arXiv:astro-ph/0607286].
 12. Stecker FW, Done C, Salamon MH, Sommers P, *Phys. Rev. Lett.* **66**:2697 (1991) [Erratum-ibid. **69**:2738 (1992)];
Stecker FW, *Phys. Rev. D* **72**:107301 (2005) [arXiv:astro-ph/0510537];
Atoyan A, Dermer CD, *Phys. Rev. Lett.* **87**:221102 (2001) [arXiv:astro-ph/0108053];
Mücke A *et al.*, *Astrop. Phys.* **18**:593 (2003);
Anchordoqui LA, Goldberg H, Halzen F, Weiler TJ, *Phys. Lett. B* **600**:202 (2004) [arXiv:astro-ph/0404387].
 13. Waxman E, Bahcall JN, *Phys. Rev. Lett.* **78**:2292 (1997) [arXiv:astro-ph/9701231];
Alvarez-Muniz J, Halzen F, Hooper DW, *Phys. Rev. D* **62**:093015 (2000) [arXiv:astro-ph/0006027];
Razzaque S, Meszaros P, Waxman E, *Phys. Rev. Lett.* **90**:241103 (2003) [arXiv:astro-ph/0212536];
Dermer CD, Atoyan A, *Phys. Rev. Lett.* **91**:071102 (2003) [arXiv:astro-ph/0301030];
Razzaque S, Meszaros P, Waxman E, *Phys. Rev. D* **68**:083001 (2003) [arXiv:astro-ph/0303505];
Becker JK, Halzen F, O’Murchadha A, Olivo M, arXiv:0911.2202 [astro-ph.HE].
 14. Berezhinsky VS, Zatsarinin GT, *Phys. Lett. B* **28**:423 (1969);
Stecker FW, *Astrophys. J.* **228**:919 (1979);
Hill CT, Schramm DN, *Phys. Lett. B* **131**:247 (1983);
Fodor Z, Katz SD, Ringwald A, Tu H, *JCAP* **0311**:015 (2003) [arXiv:hep-ph/0309171];
Allard D *et al.*, *JCAP* **0609**:005 (2006) [arXiv:astro-ph/0605327].
 15. Engel R, Seckel D, Stanev T, *Phys. Rev. D* **64**:093010 (2001) [arXiv:astro-ph/0101216].
 16. Anchordoqui LA *et al.*, *Phys. Rev. D* **76**:123008 (2007) [arXiv:0709.0734 [astro-ph]].
 17. Coleman SR, Glashow SL, *Phys. Rev. D* **59**:116008 (1999) [arXiv:hep-ph/9812418];
Fogli GL, Lisi E, Marrone A, Scioscia G, *Phys. Rev. D* **60**:053006 (1999) [arXiv:hep-ph/9904248];
Gonzalez-Garcia MC, Halzen F, Maltoni M, *Phys. Rev. D* **71**:093010 (2005) [arXiv:hep-ph/0502223];
Battistoni G *et al.*, *Phys. Lett. B* **615**, 14 (2005) [arXiv:hep-ex/0503015].
 18. Zas E, Halzen F, Vazquez RA, *Astropart. Phys.* **1**, 297 (1993);

- Gondolo P, Ingelman G, Thunman M, *Astropart. Phys.* **5**, 309 (1996) [arXiv:hep-ph/9505417];
 Costa CGS, *Astropart. Phys.* **16**, 193 (2001) [arXiv:hep-ph/0010306];
 Beacom JF, Candia J, *JCAP* **0411:009** (2004) [arXiv:hep-ph/0409046].
19. Gonzalez-Garcia MC, Halzen F, M. Maltoni M, Tanaka HKM, *Phys. Rev. Lett.* **100:061802** (2008) [arXiv:0711.0745 [hep-ph]].
 20. Anchordoqui L, Halzen F, *Annals Phys.* **321:2660** (2006) [arXiv:hep-ph/0510389].
 21. Anchordoqui LA, Feng JL, Goldberg H, Shapere AD, *Phys. Rev. D* **65:124027** (2002) [arXiv:hep-ph/0112247];
 Kusenko A, Weiler TJ, *Phys. Rev. Lett.* **88:161101** (2002) [arXiv:hep-ph/0106071].
 22. Jungman G, Kamionkowski M, *Phys. Rev. D* **51**, 328 (1995) [arXiv:hep-ph/9407351];
 Crotty P, *Phys. Rev. D* **66:063504** (2002) [arXiv:hep-ph/0205116];
 Cirelli M *et al*, *Nucl. Phys. B* **727:99** (2005) [Erratum-ibid. B **790:338** (2008)] [arXiv:hep-ph/0506298];
 Lehnert R and Weiler TJ, *Phys. Rev. D* **77:125004** (2008) [arXiv:0708.1035 [hep-ph]];
 Halzen F, Hooper D, *Phys. Rev. D* **73:123507** (2006) [arXiv:hep-ph/0510048].
 23. Anchordoqui L, Paul T, Reucroft S, Swain J, *Int. J. Mod. Phys. A* **18:2229** (2003) [arXiv:hep-ph/0206072];
 Nagano M, Watson AA, *Rev. Mod. Phys.* **72:689** (2000).
 24. Abbasi R *et al.* [HiRes Collaboration], *Phys. Rev. Lett.* **100:101101** (2008) [arXiv:astro-ph/0703099];
 Abraham J *et al.* [Pierre Auger Collaboration], *Phys. Rev. Lett.* **101:061101** (2008) [arXiv:0806.4302 [astro-ph]].
 25. Greisen K, *Phys. Rev. Lett.* **16:748** (1966);
 Zatsepin GT, Kuzmin VA, *JETP Lett.* **4:78** (1966) [*Pisma Zh. Eksp. Teor. Fiz.* **4:114** (1966)].
 26. Gaisser TK, *Cosmic Rays and Particle Physics*, Cambridge University Press, (1990).
 27. Aharonian FA, Drury LO'C, Voelk HJ, *Astron. Astrophys.* **285:645** (1994).
 28. Kelner SR, Aharonian FA, Bugayov VV, *Phys. Rev. D* **74:034018** (2006) [Erratum-ibid. D **79:039901** (2009)] [arXiv:astro-ph/0606058].
 29. Anchordoqui LA *et al.*, *Phys. Rev. D* **80:103004** (2009) [arXiv:0907.0395 [astro-ph.HE]].
 30. Abe F *et al.* [CDF Collaboration], *Phys. Rev. D* **41:2330** (1990).
 31. Torres DF *et al.*, *Phys. Rept.* **382:303** (2003) [arXiv:astro-ph/0209565].
 32. Fermi E, *Phys. Rev.* **75:1169** (1949).
 33. Anchordoqui LA *et al.*, *Phys. Rev. Lett.* **98:121101** (2007) [arXiv:astro-ph/0611580].
 34. Anchordoqui LA, Goldberg H, Halzen F, Weiler TJ, *Phys. Lett. B* **593:42** (2004) [arXiv:astro-ph/0311002].
 35. Torres DF, Anchordoqui LA, *Rept. Prog. Phys.* **67:1663** (2004) [arXiv:astro-ph/0402371].
 Olinto AV, *Phys. Rept.* **333:329** (2000) [arXiv:astro-ph/0002006].
 36. Bergman DR *et al* [HiRes Collaboration], astro-ph/0407244.
 37. Bird DJ *et al.* [Fly's Eye Collaboration], *Phys. Rev. Lett.* **71:3401** (1993).
 38. Berezhinsky V, Gazizov AZ, Grigorieva SI, *Phys. Rev. D* **74:043005** (2006).

- [arXiv:hep-ph/0204357].
39. Ahlers M *et al.*, *Phys. Rev. D* **72**:023001 (2005) [arXiv:astro-ph/0503229].
 40. Waxman E, *Astrophys. J.* **452**:L1 (1995) [arXiv:astro-ph/9508037].
 41. Gaisser TK, arXiv:astro-ph/9707283.
 42. Waxman E, Bahcall JN, *Phys. Rev. D* **59**:023002 (1999) [arXiv:hep-ph/9807282].
 43. Anchordoqui LA, Goldberg H, Halzen F, Weiler TJ, *Phys. Lett. B* **621**:18 (2005) [arXiv:hep-ph/0410003].
 44. Stecker FW, *Phys. Rev. Lett.* **21**:1016 (1968).
 45. Alvarez-Muniz J *et al.*, *Phys. Rev. D* **66**:033011 (2002) [arXiv:astro-ph/0205302].
 46. Learned JG, Pakvasa S, *Astropart. Phys.* **3**:267 (1995) [arXiv:hep-ph/9405296].
 47. Kashti T, Waxman E, *Phys. Rev. Lett.* **95**:181101 (2005) [arXiv:astro-ph/0507599];
Lipari P, Lusignoli M, Meloni D, *Phys. Rev. D* **75**:123005 (2007) [arXiv:0704.0718 [astro-ph]];
Pakvasa S, Rodejohann W and Weiler TJ, *JHEP* **0802**:005 (2008) [arXiv:0711.4517 [hep-ph]].
 48. Anchordoqui LA, Hooper D, Sarkar S, Taylor AM, *Astropart. Phys.* **29**:1 (2008) [arXiv:astro-ph/0703001].
 49. Hooper D, Taylor A, Sarkar S, *Astropart. Phys.* **23**:11 (2005) [arXiv:astro-ph/0407618];
Ave M *et al.*, *Astropart. Phys.* **23**:19 (2005) [arXiv:astro-ph/0409316];
Hooper D, Sarkar S, Taylor AM, *Phys. Rev. D* **77**:103007 (2008) [arXiv:0802.1538 [astro-ph]].
 50. Amsler C *et al.* [Particle Data Group], *Phys. Lett. B* **667**:1 (2008).
 51. Markov MA, Proceedings of 10th International Conference on High Energy Physics, Rochester, ed. E. C. G. Sudarshan *et al.*, p. 578 (1960);
Markov MA, Zheleznykh IM, *Nucl. Phys.* **27**:385 (1961).
 52. Sinegovskaya TS, Sinegovsky SI, *Phys. Rev. D* **63**:096004 (2001) [arXiv:hep-ph/0007234];
Carminati G, Margiotta A, Spurio M, *Nucl. Instrum. Meth. A* **602**:95 (2009).
 53. Bazzotti M for the ANTARES Collaboration, Proceedings of the 31st International Cosmic Ray Conference (ICRC2009), HE 2.1 0340;
Desiati P for the AMANDA Collaboration, Proceedings of the 28th Int. Cosmic Ray Conference (ICRC2003), Tsukuba:1373.
 54. Belolaptikov IA *et al.* [BAIKAL Collaboration], *Astropart. Phys.* **7**:263 (1997).
 55. Babson J *et al.* [DUMAND Collaboration], *Phys. Rev. D* **42**:3613 (1990).
 56. Aggouras G *et al.* [NESTOR Collaboration], *Astropart. Phys.* **23**:377 (2005).
 57. Chirkin D for the IceCube Collaboration, ICRC2009, HE 2.2 1418.
 58. Honda M *et al.*, *Phys. Rev. D* **75**:043006 (2007) [arXiv:astro-ph/0611418].
 59. Martin AD, Ryskin MG, Stasto AM, *Acta Phys. Polon. B* **34**:3273 (2003) [arXiv:hep-ph/0302140].
 60. Enberg R, Reno MH, Sarcevic I, *Phys. Rev. D* **78**:043005 (2008) [arXiv:0806.0418 [hep-ph]].
 61. Fiorentini G, Naumov VA, Villante FL, *Phys. Lett. B* **510**:173 (2001) [arXiv:hep-ph/0103322];

- Bugaev EV, Naumov VA, Sinegovsky SI, Zaslavskaya ES, *Nuovo Cim. C* **12**, 41 (1989);
Bugaev EV, *Phys. Rev. D* **58**:054001 (1998) [arXiv:hep-ph/9803488].
62. Glashow SL, *Phys. Rev.* **118**:316 (1960).
63. Gandhi R, Quigg C, Reno MH, Sarcevic I, *Astropart. Phys.* **5**:81 (1996) [arXiv:hep-ph/9512364]; Gandhi R, Quigg C, Reno MH, Sarcevic I, *Phys. Rev. D* **58**:093009 (1998) [arXiv:hep-ph/9807264];
Anchordoqui LA, Cooper-Sarkar AM, Hooper D, Sarkar S, *Phys. Rev. D* **74**:043008 (2006) [arXiv:hep-ph/0605086];
Cooper-Sarkar A, Sarkar S, *JHEP* **0801**:075 (2008) [arXiv:0710.5303 [hep-ph]].
64. L'Abbate A, Montaruli T, Sokalski I, *Astropart. Phys.* **23**:57 (2005) [arXiv:hep-ph/0406133].
65. Halzen F, Saltzberg D, *Phys. Rev. Lett.* **81**:4305 (1998) [arXiv:hep-ph/9804354].
66. Bugaev E, Montaruli T, Shlepin Y, Sokalski I, *Astropart. Phys.* **21**:491 (2004) [arXiv:hep-ph/0312295].
67. DUMAND Proposal, Report No. HDC-3-88 (unpublished, 1980).
68. Bezrukov LB *et al.*, Proceedings of the International Conference “Neutrino-84”, World Sci. Publ., Singapore, 550 (1984).
69. Kuzmichev L *et al.* [Baikal Collaboration], ICRC2009, id number: 1091,
70. Halzen F *et al.*, 4th International Symposium on Neutrino Telescopes, Venice, Italy, 10-13 Mar 1992.
71. Andres E *et al.*, *Astropart. Phys.* **13**:1 (2000) [arXiv:astro-ph/9906203];
Andres E *et al.*, *Nature* **410**:441 (2001).
72. Abbasi R *et al.* [IceCube Collaboration], *Nucl. Instrum. Meth. A* **601**:294 (2009) [arXiv:0810.4930 [physics.ins-det]].
73. Achterberg A *et al.* [IceCube Collaboration], *Astropart. Phys.* **26**:155 (2006) [arXiv:astro-ph/0604450].
74. Amram P *et al.* [ANTARES Collaboration], *Astropart. Phys.* **19**:253 (2003) [arXiv:astro-ph/0206454];
Amram P *et al.* [ANTARES Collaboration], *Astropart. Phys.* **13**:127 (2000) [arXiv:astro-ph/9910170];
Aguilar JA *et al.* [ANTARES Collaboration], *Astropart. Phys.* **23**:131 (2005) [arXiv:astro-ph/0412126].
75. Aguilar JA *et al.* [ANTARES Collaboration], *Astropart. Phys.* **26**:314 (2006);
Aguilar JA *et al.* [ANTARES Collaboration], *Nucl. Instrum. Meth. A* **581**:695 (2007).
76. Aguilar JA *et al.* [ANTARES Collaboration], *Nucl. Instrum. Meth. A* **555**:132 (2005).
77. Aguilar JA *et al.* [ANTARES Collaboration], *Nucl. Instrum. Meth. A* **484**:369 (2002).
78. Aguilar JA *et al.* [ANTARES Collaboration], *Nucl. Instrum. Meth. A* **578**:498 (2007).
79. Aguilar JA *et al.* [ANTARES Collaboration], *Nucl. Instrum. Meth. A* **570**:107 (2007).
80. Abbasi R. *et al.* [IceCube Collaboration], *Phys. Rev. D* **79**:062001 (2009) [arXiv:0809.1646 [astro-ph]].
81. Montaruli T, *Nucl. Phys. Proc. Suppl.* **190**:101 (2009) [arXiv:0901.2661

- [astro-ph]].
82. Sapienza P, Coniglione R, Distefano C, Migneco E, *Nucl. Instrum. Meth. A* **602**, 101 (2009).
 83. Dumm J. *et al.*, ICRC2009, OG 2.5 0653.
 84. Katz UF, *Nucl. Instrum. Meth. A* **567**:457 (2006) [arXiv:astro-ph/0606068].
 85. Montaruli T, arXiv:0910.4364 [hep-ph].
 86. Halzen F, Jacobsen JE, Zas E, *Phys. Rev. D* **53**:7359 (1996) [arXiv:astro-ph/9512080].
 87. Berezhinsky VS, Smirnov AY, *Phys. Lett. B* **48**:269 (1974);
Capelle KS, Cronin JW, Parente G, Zas E, *Astropart. Phys.* **8**:321 (1998) [arXiv:astro-ph/9801313];
Anchordoqui L *et al.*, *Annals Phys.* **314**:145 (2004) [arXiv:hep-ph/0407020].
 88. Bertou X *et al.*, *Astropart. Phys.* **17**:183 (2002) [arXiv:astro-ph/0104452];
Feng JL, Fisher P, Wilczek F, Yu TM, *Phys. Rev. Lett.* **88**:161102 (2002) [arXiv:hep-ph/0105067];
Fargion D, *Astrophys. J.* **570**:909 (2002) [arXiv:astro-ph/0002453].
 89. Boersma D, Gladstone L, Karle A, for the IceCube Collaboration, ICRC2009, OG 2.5.1173.
 90. Borriello E *et al.*, *Nucl. Phys. Proc. Suppl.* **190**:150 (2009).
 91. Ambrosio M *et al.* [MACRO Collaboration], *Astrophys. J.* **546**:1038 (2001) [arXiv:astro-ph/0002492];
Oyama Y *et al.* [KAMIOKANDE-II Collaboration], *Phys. Rev. D* **39**: 1481 (1989);
Berger C *et al.* [Frejus Collaboration], *Z. Phys. C* **48**:221 (1990);
Abe K *et al.* [Super-Kamiokande Collaboration], *Astrophys. J.* **652**:198 (2006) [arXiv:astro-ph/0606413];
Desai S *et al.* [Super-Kamiokande Collaboration], *Astropart. Phys.* **29**:42 (2008) [arXiv:0711.0053 [hep-ex]];
Achterberg A *et al.* [IceCube Collaboration], *Phys. Rev. D* **75**:102001 (2007) [arXiv:astro-ph/0611063].
 92. Abbasi R. *et al.* [IceCube Collaboration], *Astrophys. J.* **701**:L47 (2009) [arXiv:0905.2253 [astro-ph.HE]];
Thrane E *et al.* [Super-Kamiokande Collaboration], *Astrophys. J.* **704**:503 (2009) [arXiv:0907.1594 [astro-ph.HE]];
Abbasi R, *et al.* [IceCube Collaboration], *Astrophys. J.* **701**: 1721 (2009);
 93. Braun J *et al.*, *Astropart. Phys.* **29**:299 (2008) [arXiv:0801.1604 [astro-ph]];
Aguilar JA, Hernandez-Rey JJ, *Astropart. Phys.* **29**:117 (2008);
Alexandreas DE *et al.*, *Nucl. Instrum. Meth. A* **328**:570 (1993);
Braun J, in preparation.
 94. Abbasi R *et al.* [The IceCube Collaboration], *Phys. Rev. Lett.* **103**:221102 (2009) [arXiv:0911.2338 [astro-ph.HE]].
 95. Gaisser TK, Honda M, *Ann. Rev. Nucl. Part. Sci.* **52**:153 (2002) [arXiv:hep-ph/0203272].
 96. Gonzalez-Garcia MC, Maltoni M, *Phys. Rept.* **460**:1 (2008) [arXiv:0704.1800 [hep-ph]].
 97. Lipari P, *Astropart. Phys.* **1**, 195 (1993).
 98. Barr GD *et al.*, *Phys. Rev. D* **70**:023006 (2004) [arXiv:astro-ph/0403630].
 99. Battistoni G *et al.*, *Astropart. Phys.* **12**:315 (2000) [arXiv:hep-ph/9907408].
 100. Barr GD, Gaisser TK, Robbins S, Stanev T, *Phys. Rev. D* **74**:094009 (2006) [arXiv:astro-ph/0611266].

101. Berghaus P, Montaruli T, Ranft J, *JCAP* **0806**:003 (2008) [arXiv:0712.3089 [hep-ex]].
102. D'Alessandro R *et al.*, *Nucl. Phys. Proc. Suppl.* **190**:52 (2009);
Anelli G *et al.* [TOTEM Collaboration], *JINST* **3**:S08007 (2008).
103. Ahn EJ, arXiv:0906.4113 [hep-ph];
Ostapchenko S, *AIP Conf. Proc.* **928**:118 (2007) [arXiv:0706.3784 [hep-ph]];
Kochanov AA, Sinegovskaya TS, Sinegovsky SI, ICRC2009, OG 2.5 0693;
Berghaus P *et al.*, in Neutrino 2008 proceedings, New Zealand.
104. Adamson P *et al.* [MINOS Collaboration], *Phys. Rev. D* **76**:052003 (2007) [arXiv:0705.3815 [hep-ex]].
105. Abbasi R *et al.* [IceCube Collaboration], *Phys. Rev. D* **79**:102005 (2009) [arXiv:0902.0675 [astro-ph.HE]].
106. Abbasi R *et al.* [IceCube Collaboration], arXiv:0907.0498 [astro-ph.HE].
107. Amenomori M [Tibet AS-gamma Collaboration], *Science* **314**:439 (2006) [arXiv:astro-ph/0610671].
108. Abdo AA *et al.*, *Astrophys. J.* **698**, 2121 (2009) [arXiv:0806.2293 [astro-ph]];
A. A. Abdo *et al.*, *Phys. Rev. Lett.* **101**, 221101 (2008) [arXiv:0801.3827 [astro-ph]];
Guillian G *et al.* [Super-Kamiokande Collaboration], *Phys. Rev. D* **75**:062003 (2007) [arXiv:astro-ph/0508468];
Zhang JL *et al.*, ICRC2009, HE 1.1 0814;
Vernetto S *et al.*, ICRC2009, OG 2.3 0399.
109. Compton AH, Getting IA, *Phys. Rev.* **47**:817 (1935).
110. Salvati M, Sacco B, arXiv:0802.2181 [astro-ph];
Drury L and Aharonian F, *Astropart. Phys.* **29**:420 (2008) [arXiv:0802.4403 [astro-ph]];
Erlykin AD and Wolfendale AW, arXiv:0906.3949 [hep-ph].
111. Adriani O *et al.* [PAMELA Collaboration], *Nature* **458**:607 (2009) [arXiv:0810.4995 [astro-ph]];
Chang J *et al.*, *Nature* **456**:362 (2008);
Aharonian F *et al.* [H.E.S.S. Collaboration], *Phys. Rev. Lett.* **101**:261104 (2008) [arXiv:0811.3894 [astro-ph]];
Abdo AA *et al.* [The Fermi LAT Collaboration], *Phys. Rev. Lett.* **102**, 181101 (2009) [arXiv:0905.0025 [astro-ph.HE]].
112. Hooper D, Blasi P, Serpico PD, *JCAP* **0901**:025 (2009) [arXiv:0810.1527 [astro-ph]];
Yuksel H, Kistler MD, Stanev T, *Phys. Rev. Lett.* **103**:051101 (2009) [arXiv:0810.2784 [astro-ph]];
Blasi P, *Phys. Rev. Lett.* **103**:051104 (2009) [arXiv:0903.2794 [astro-ph.HE]];
Mertsch P, Sarkar S., *Phys. Rev. Lett.* **103**:081104 (2009) [arXiv:0905.3152 [astro-ph.HE]];
Ahlers M, Mertsch P, Sarkar S, arXiv:0909.4060 [astro-ph.HE].
113. Butt Y, *Nature* **460**:701 (2009).
114. Coyle P for the ANTARES Collaboration, ICRC2009, highlight talk.
115. Achterberg A *et al.* [IceCube Collaboration], *Phys. Rev. D* **76**:042008 (2007) [Erratum-ibid. D **77**:089904 (2008)] [arXiv:0705.1315 [astro-ph]].
116. Ahrens J *et al.* [IceCube Collaboration], *Astropart. Phys.* **20**:507 (2004) [arXiv:astro-ph/0305196].
117. Abraham J *et al.* [Pierre Auger Collaboration], arXiv:0906.2347;

- Abraham J *et al.* [Pierre Auger Collaboration], *Phys. Rev. D* **79**:102001 (2009) [arXiv:0903.3385 [astro-ph.HE]];
- Abraham J *et al.* [Pierre Auger Collaboration], *Phys. Rev. Lett.* **100**:211101 (2008) [arXiv:0712.1909 [astro-ph]].
118. Abbasi R *et al.*, in preparation.
119. Silvestri S *et al.*, ICRC2009, OG 2.5 0549.
120. Mase K, Ishihara A, Yoshida S for the IceCube Collaboration, ICRC2009, HE 1.4 0861.
121. Abbasi RU *et al.*, arXiv:0803.0554 [astro-ph];
Gorham PW *et al.* [ANITA collaboration], *Phys. Rev. Lett.* **103**, 051103 (2009) [arXiv:0812.2715 [astro-ph]];
James CW *et al.*, arXiv:0907.4332 [astro-ph.HE];
Kravchenko I *et al.*, *Phys. Rev. D* **73**:082002 (2006) [arXiv:astro-ph/0601148].
122. Ahlers M, Anchordoqui LA, Sarkar S, *Phys. Rev. D* **79**:083009 (2009) [arXiv:0902.3993 [astro-ph.HE]].
123. Hopkins AM, Beacom JF, *Astrophys. J.* **651**:142 (2006) [arXiv:astro-ph/0601463].
124. Hasinger G, Miyaji T, Schmidt M, *Astron. Astrophys.* **441**:417 (2005) [arXiv:astro-ph/0506118];
Stanev T, arXiv:0808.1045 [astro-ph].
125. Anchordoqui LA *et al.* [Pierre Auger Collaboration], arXiv:0907.5208 [astro-ph.HE].
126. Riess AG *et al.* [Supernova Search Team Collaboration], *Astron. J.* **116**:1009 (1998) [arXiv:astro-ph/9805201];
Perlmutter S *et al.* [Supernova Cosmology Project Collaboration], *Astrophys. J.* **517**:565 (1999) [arXiv:astro-ph/9812133];
E. Komatsu *et al.* [WMAP Collaboration], *Astrophys. J. Suppl.* **180**:330 (2009) [arXiv:0803.0547 [astro-ph]];
Colless M *et al.*, arXiv:astro-ph/0306581;
Tegmark M *et al.* [SDSS Collaboration], *Phys. Rev. D* **69**:103501 (2004) [arXiv:astro-ph/0310723];
Reid BA *et al.*, arXiv:0907.1659 [astro-ph.CO].
127. Burles S, Nollett KM, Turner MS, *Astrophys. J.* **552**:L1 (2001) [arXiv:astro-ph/0010171];
Cyburt RH, Fields BD, Olive KA, *Phys. Lett. B* **567**:227 (2003) [arXiv:astro-ph/0302431].
128. Bergstrom L, *Rept. Prog. Phys.* **63**:793 (2000) [arXiv:hep-ph/0002126];
Bertone G, Hooper D, Silk J, *Phys. Rept.* **405**:279 (2005) [arXiv:hep-ph/0404175];
Feng JL, *J. Phys. G* **32**:R1 (2006) [arXiv:astro-ph/0511043].
129. Goldberg H, *Phys. Rev. Lett.* **50**:1419 (1983);
Ellis JR *et al.*, *Nucl. Phys. B* **238**:453 (1984).
130. Servant G, Tait TMP, *Nucl. Phys. B* **650**:391 (2003) [arXiv:hep-ph/0206071];
Cheng HC, Feng JL, Matchev KT, *Phys. Rev. Lett.* **89**:211301 (2002) [arXiv:hep-ph/0207125].
131. Scherrer RJ, Turner MS, *Phys. Rev. D* **33**:1585 (1986) [Erratum-ibid. *D* **34**:3263 (1986)].
132. Griest K, Kamionkowski M, Turner MS, *Phys. Rev. D* **41**:3565 (1990);
Drees M, Nojiri MM, *Phys. Rev. D* **47**:376 (1993) [arXiv:hep-ph/9207234];

- Birkedal-Hansen A, Jeong Eh, *JHEP* **0302**:047 (2003) [arXiv:hep-ph/0210041].
133. Goodman MW, Witten E, *Phys. Rev. D* **31**:3059 (1985).
134. Silk J, Olive KA, Srednicki M, *Phys. Rev. Lett.* **55**:257 (1985);
Srednicki M, Olive KA, Silk J, *Nucl. Phys. B* **279**:804 (1987);
Ng KW, Olive KA, Srednicki M, *Phys. Lett. B* **188**:138 (1987);
Bergstrom L, Edsjo J, Gondolo P, *Phys. Rev. D* **58**:103519 (1998) [arXiv:hep-ph/9806293];
Feng JL, Matchev KT, Wilczek F, *Phys. Rev. D* **63**:045024 (2001) [arXiv:astro-ph/0008115];
Barger VD, Halzen F, Hooper D, Kao C, *Phys. Rev. D* **65**:075022 (2002) [arXiv:hep-ph/0105182].
135. Rudaz S, Stecker FW, *Astrophys. J.* **368**:406 (1991);
Bergstrom L, Ullio P, Buckley JH, *Astropart. Phys.* **9**:137 (1998) [arXiv:astro-ph/9712318];
Dodelson S, Hooper D, Serpico PD, *Phys. Rev. D* **77**:063512 (2008) [arXiv:0711.4621 [astro-ph]];
Bertone G *et al.*, *Phys. Rev. D* **80**:023512 (2009) [arXiv:0904.1442 [astro-ph.HE]];
Goodenough L, Hooper D, arXiv:0910.2998 [hep-ph];
Anchordoqui L *et al.*, arXiv:0912.0517 [hep-ph].
136. Navarro JF, Frenk CS, White SDM, *Astrophys. J.* **490**:493 (1997) [arXiv:astro-ph/9611107].
137. Aharonian FA *et al.* [H.E.S.S. Collaboration], *Phys. Rev. Lett.* **97**:221102 (2006) [Erratum-ibid. **97**:249901 (2006)] [arXiv:astro-ph/0610509].
138. Aharonian F *et al.* [H.E.S.S. Collaboration], *Nature* **439**:695 (2006) [arXiv:astro-ph/0603021].
139. Gould A, *Astrophys. J.* **388**:338 (1992);
Jungman G, Kamionkowski M, Griest K, *Phys. Rept.* **267**:195 (1996) [arXiv:hep-ph/9506380].
140. Griest K, Seckel D, *Nucl. Phys. B* **283**:681 (1987) [Erratum-ibid. B **296**:1034 (1988)]. Gould A, *Astrophys. J.* **321**:560 (1987).
141. Ahmed Z *et al.* [CDMS Collaboration], *Phys. Rev. Lett.* **102**:011301 (2009) [arXiv:0802.3530 [astro-ph]].
142. Angle J *et al.* [XENON Collaboration], *Phys. Rev. Lett.* **100**:021303 (2008) [arXiv:0706.0039 [astro-ph]].
143. Tanaka T for the Super-Kamiokande Collaboration, ICRC2009, HE 2.3 0622;
Desai S *et al.* [Super-Kamiokande Collaboration], *Phys. Rev. D* **70**:083523 (2004) [Erratum-ibid. D **70**:109901 (2004)] [arXiv:hep-ex/0404025].
144. Ambrosio M *et al.* [MACRO Collaboration], *Phys. Rev. D* **60**:082002 (1999) [arXiv:hep-ex/9812020].
145. Braun J, Hubert D for the IceCube Collaboration, ICRC2009, HE 2.3 0834.
146. Avrorin A *et al.*, ICRC2009, HE 2.3 1165.
147. Abbasi R *et al.* [IceCube Collaboration], *Phys. Rev. Lett.* **102**:201302 (2009) [arXiv:0902.2460 [astro-ph.CO]].
148. Lim GMA for the ANTARES Collaboration, ICRC2009, HE 2.3 0031.
149. Behnke E *et al.* [COUPP Collaboration], *Science* **319**:933 (2008) [arXiv:0804.2886 [astro-ph]];
Lee HS *et al.* [KIMS Collaboration], *Phys. Rev. Lett.* **99**:091301 (2007)

- [arXiv:0704.0423 [astro-ph]].
150. Gondolo P *et al.*, *JCAP* **0407**:008 (2004) [arXiv:astro-ph/0406204].

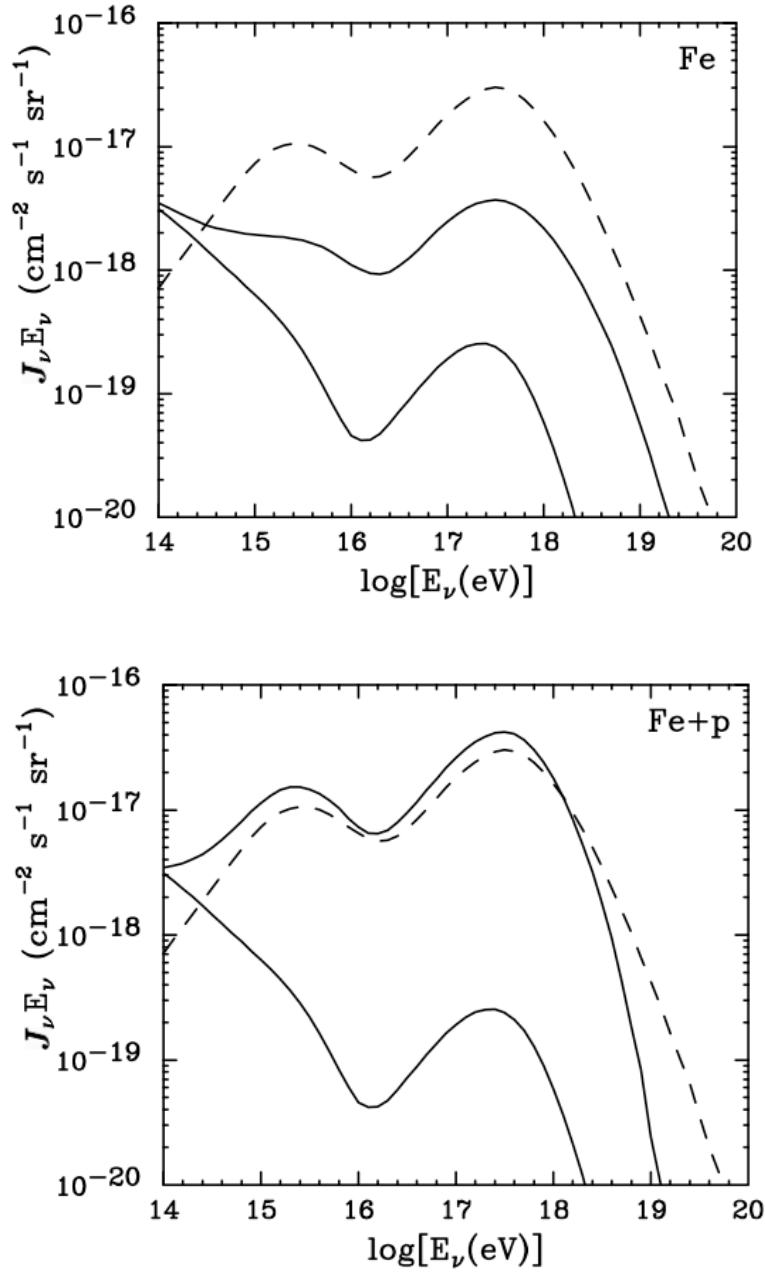


Figure 1: The solid lines indicate the range for the cosmogenic neutrino spectrum for $\alpha = 1.4 - 3.0$ and $E_{\text{max}}/Z = 10^{21} - 10^{22}$ eV, for pure iron (up) and iron and proton (down). In each frame, we show for comparison as a dashed curve the prediction for an all-proton spectrum with $\alpha = 2.2$ and $E_{\text{max}} = 10^{22}$ eV (16).

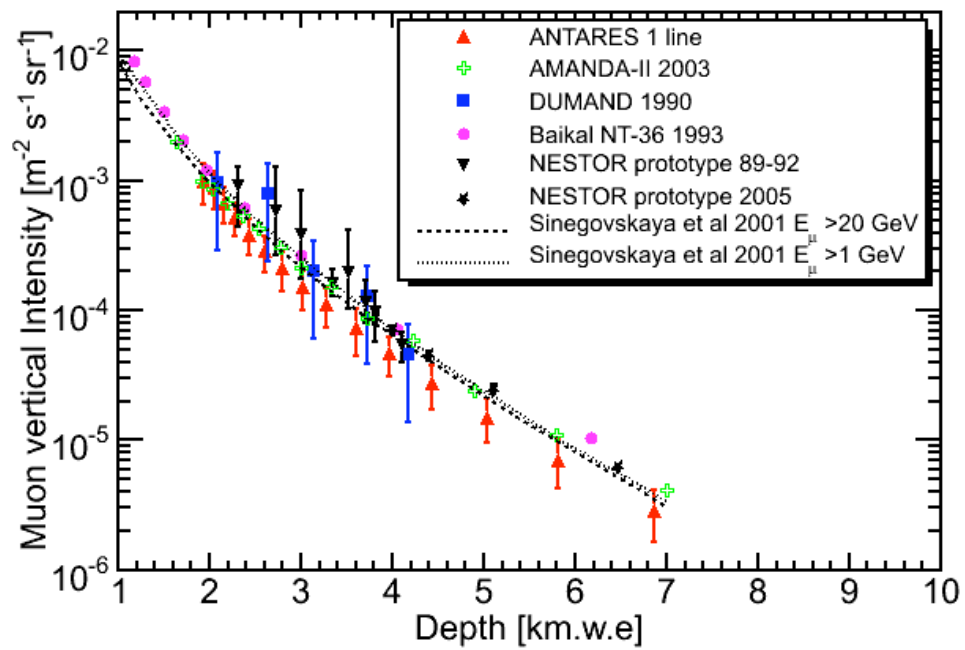


Figure 2: Atmospheric muon vertical intensity measured by under-water and ice arrays as a function of depth compared to calculations (52). No correction is applied for the slightly different muon propagation properties between water and ice. Data are from: ANTARES and AMANDA-II (53), Baikal, NT-36 (54), the DUMAND prototype string (55), and NESTOR (for 2 different prototypes) (56).

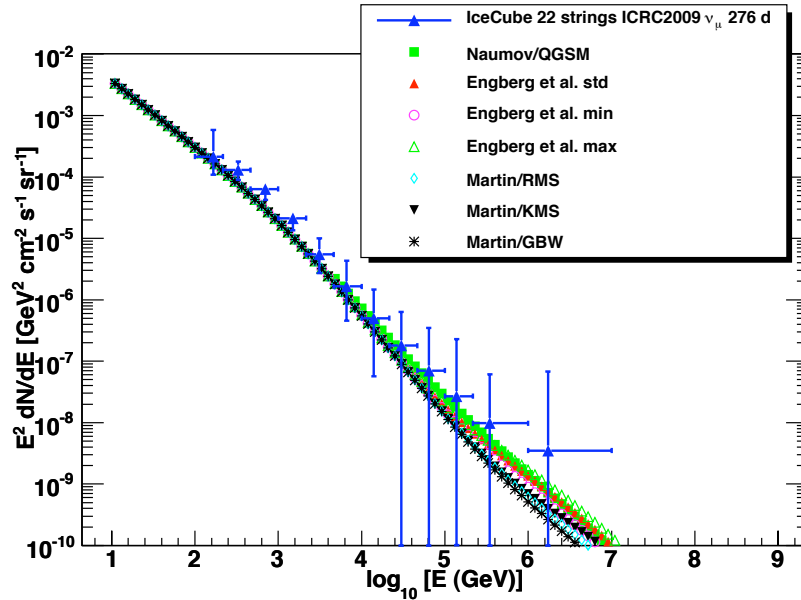


Figure 3: Preliminary atmospheric unfolded neutrino spectrum measured with 22 strings of IceCube (57) compared with predictions for $\nu_\mu + \bar{\nu}_\mu/3$. (The factor $1/3$ accounts for the lower CC interaction cross section of anti-neutrinos up to about 10^5 GeV compared to neutrinos.) Data are accompanied by large error bars. A preliminary evaluation of systematic errors, which are mainly due to the ice purity level dependence with depth, is included in the error bars. The energy bin size was selected to match the energy resolution of the experiment. (Since the energy resolution is 0.3 on the $\log_{10}(E_\mu)$, there are 3 bins per decade.) The size of the last 2 bins is larger, and determined by the desire to accommodate bins with vanishing contents. Conventional neutrino fluxes are calculated as in (58), prompt models are calculated in the framework of perturbative-QCD in (60) (std stands for optimal parameters, whereas min and max indicate the range of variation of the model parameters) and in (59) for different structure functions; the Quark-Gluon String model (QGSM) (61) is also shown.

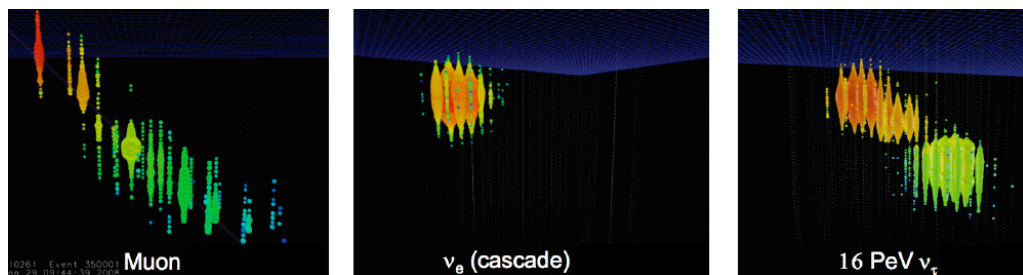


Figure 4: Simulated events in the IceCube detector, visualized using the IceCube event display, showing the 3 typical topologies discussed in Sec 3. The shading represents the time sequence of the hits. The size of the dots corresponds to the number of photoelectrons detected by the individual photomultipliers. From left to right: a muon event of 100 TeV, a cascade event induced by a 100 TeV ν_e , and a double bang event induced by a 16 PeV ν_τ .

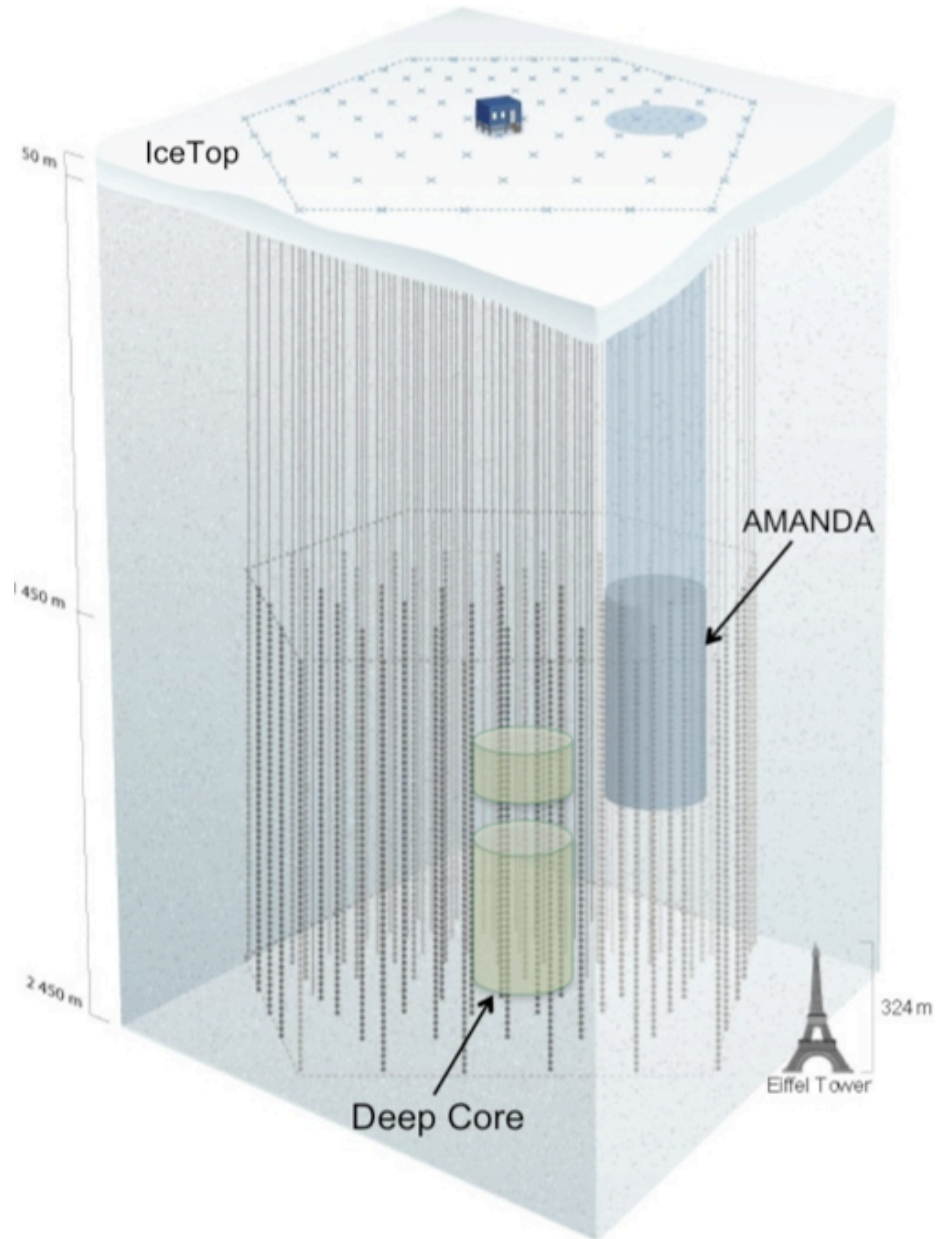


Figure 5: The IceCube Observatory, including the deep ice array, IceTop, AMANDA, and Deep Core. For comparing sizes the image of the Eiffel tower is also shown.

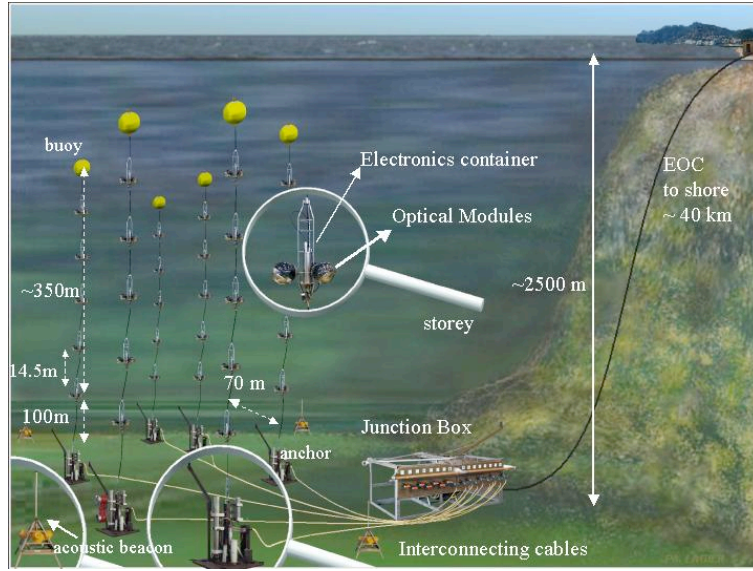


Figure 6: A pictorial view of the ANTARES detector including an insert of a storey.

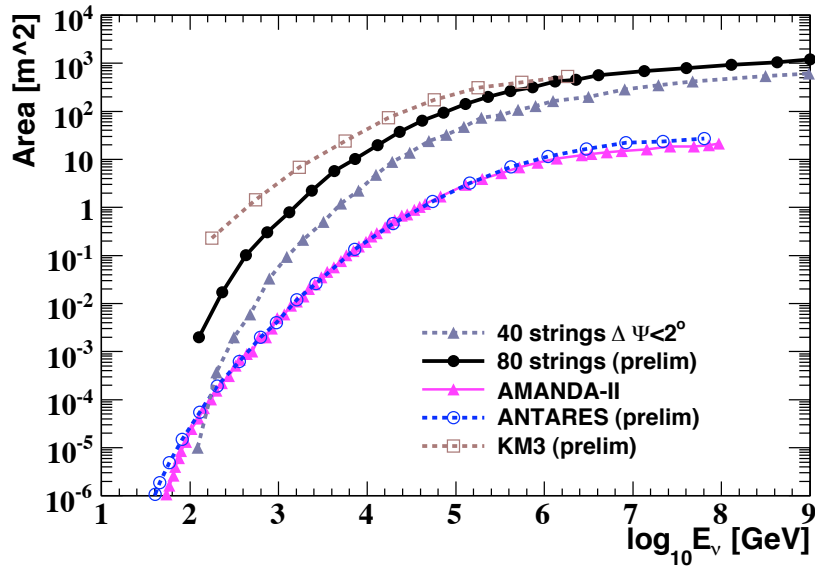


Figure 7: Effective area for muon neutrinos, integrated over the lower hemisphere, as a function of the neutrino energy. The selected cuts ensure a pointing capability suitable for point source searches. The area for 40 strings of IceCube is obtained with the requirement that tracks are reconstructed inside 2° from a source. The full IceCube area is obtained using the same cuts, and is therefore preliminary. The AMANDA-II area is from the final analysis in Ref. (80). The ANTARES effective area is obtained with preliminary selection cuts based on simulation (81). The KM3NeT area is for a possible configuration still under debate (82).

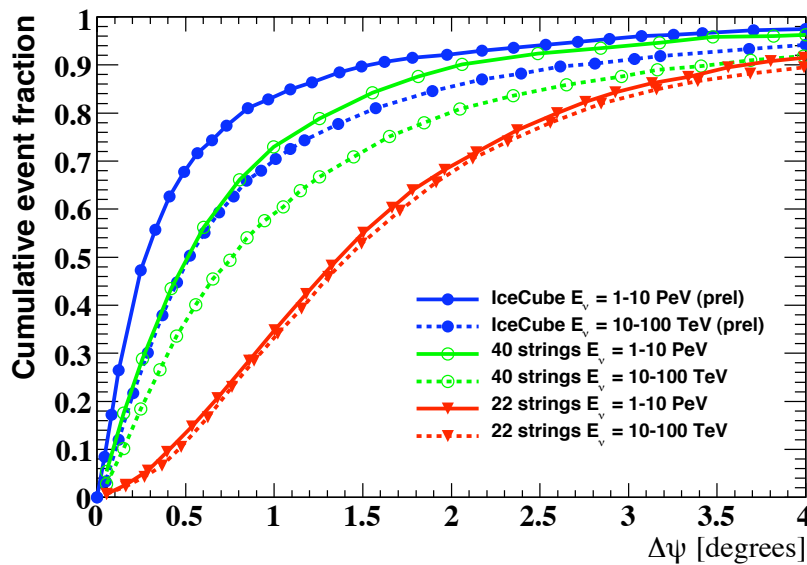


Figure 8: Cumulative distribution of reconstructed muon events inside a cone of semi-angle $\Delta\Psi$ (Point Spread Function) from the neutrino direction. The different curves indicate growing configurations of IceCube for two neutrino energy bins and the point-source analysis cuts (83). The IceCube curves are preliminary, because they are based on cuts optimized for the 40 string analysis.

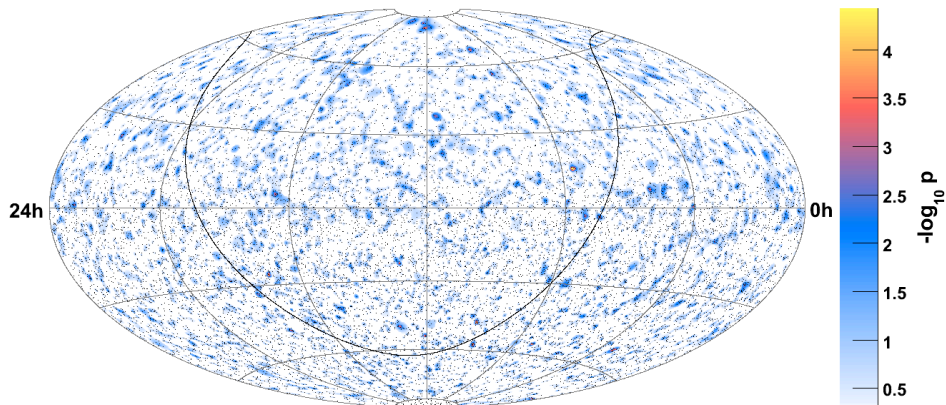


Figure 9: Muon event skymap (z -axis color code is pre-trial significance) for six months of data taken with the 40-string IceCube array, from July 2008 through December 2008. Of the 17777 black dots on the skymap, 6797 are upgoing neutrino candidates (zenith $> 90^\circ$) from the northern hemisphere. The color shading indicates the significance of the data and the curved black line is the galactic plane (83).

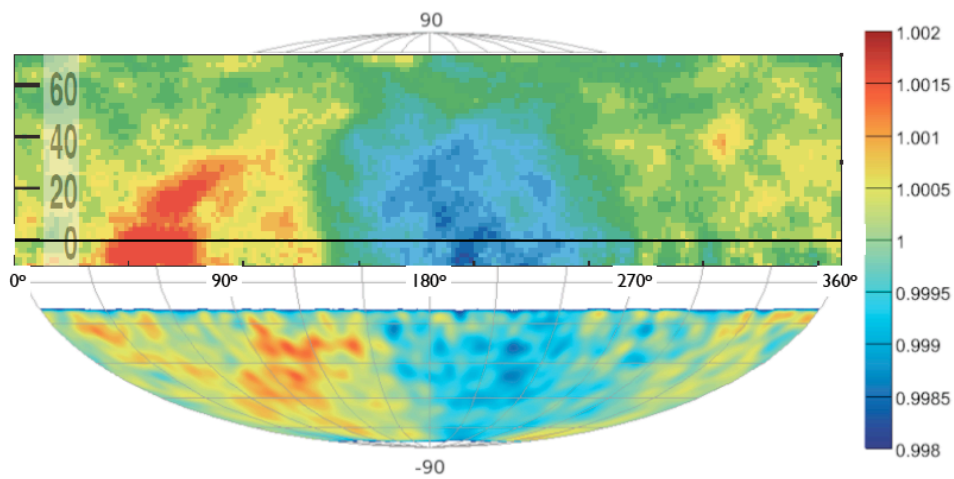


Figure 10: Upper panel: Celestial cosmic ray intensity map for Tibet AS γ data taken from 2001-5. The vertical color bin width for the relative intensity, that is calculated within each declination band, is 2.5×10^{-4} (107). The highest and lowest intensities are observed in the region of the tail-in and loss-cone in the direction of the heliotail, and on the right the excess is in the direction of Cygnus. Lower panel: Downward going muon skymap (expressed as relative intensity \equiv number of events in an angular bin in right ascension and declination divided by the total number of events in the declination band) observed by 22 strings of the IceCube neutrino telescope with data taken between April 2006-7 (106).

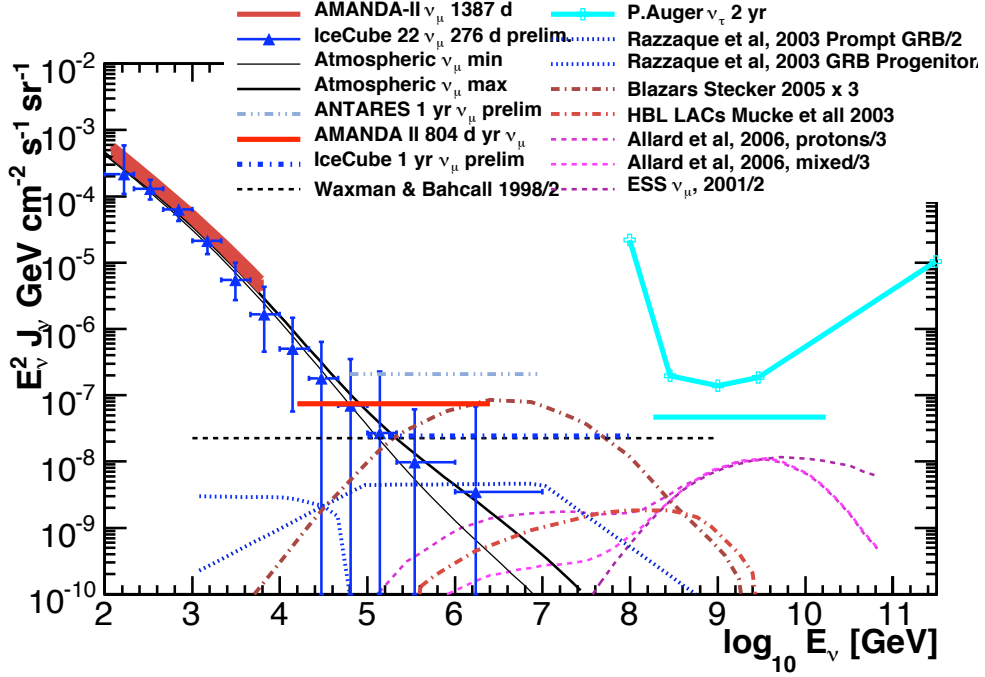


Figure 11: The blue triangles indicate the atmospheric ($\nu_\mu + \bar{\nu}_\mu$) flux averaged over the lower hemisphere as measured by 22 strings of IceCube (57)), and the falling thick solid line indicates AMANDA-II measurements (105)). For comparison, predictions of the atmospheric neutrino flux (conventional + prompt) are indicated by the falling thin solid lines (58, 60, 61, 98). The horizontal lines represent different 90%CL limits and sensitivities on E_ν^{-2} fluxes; from top to bottom: ANTARES estimated sensitivity for 1 yr (114), AMANDA-II muon neutrino limit for 804 days (115), IceCube estimated sensitivity for 1 yr (116). For comparison, also shown are (i) the Waxman and Bahcall upper limit corrected for oscillations (42), (ii) neutrino flux predictions from AGNs (12) and prompt and precursor emission from GRBs (13), and (iii) various estimates of the nearly guaranteed cosmogenic flux (14,15). The ultra-high energy upper limit on the tau neutrino flux (differential and $\propto E_\nu^{-2}$) reported by the Pierre Auger Collaboration is also shown (117).

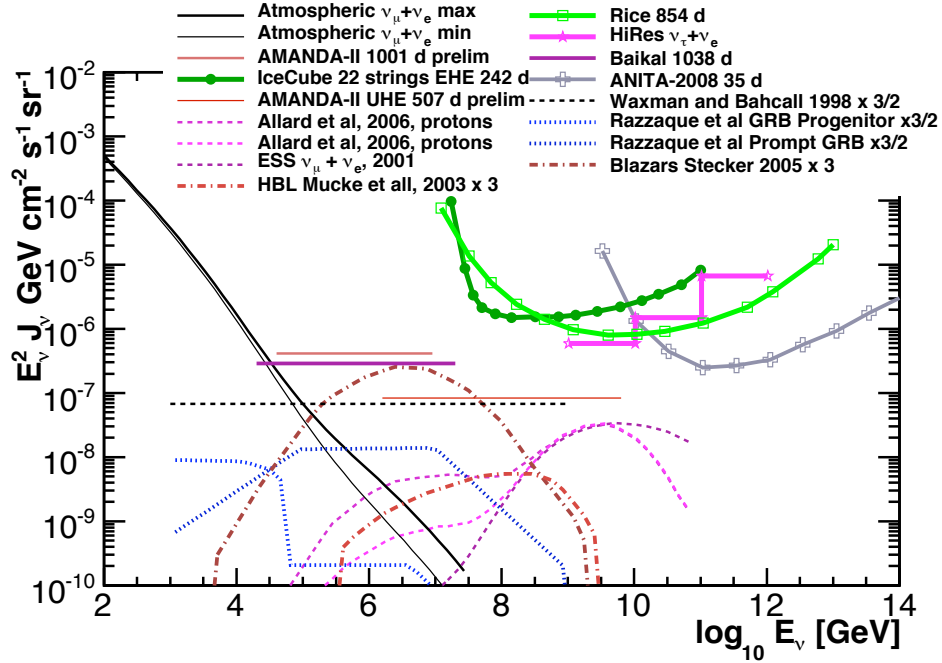


Figure 12: Same as in Fig. 11 but for experiments measuring more than one flavor, e.g. measuring cascades induced by all flavor neutrinos. The horizontal solid lines are 90%CL limits for a flux $\propto E_\nu^{-2}$; from top to bottom: AMANDA-II all-flavor cascade limit for 1001 days (118), Baikal cascade limit for 1038 days (69), AMANDA-II muon neutrino limit for 804 days (115), all flavor ultra-high energy limit (preliminary) for 507 days of AMANDA-II (119). The differential in energy upper limits (90% CL) are for the 22 strings of IceCube (120) and several ultra-high energy neutrino detection experiments, including those with radio detectors that look for the coherent Cherenkov radiation produced by the excess of electrons in neutrino induced showers in dense media (e.g., ice and the lunar regolith). For further details see (85).

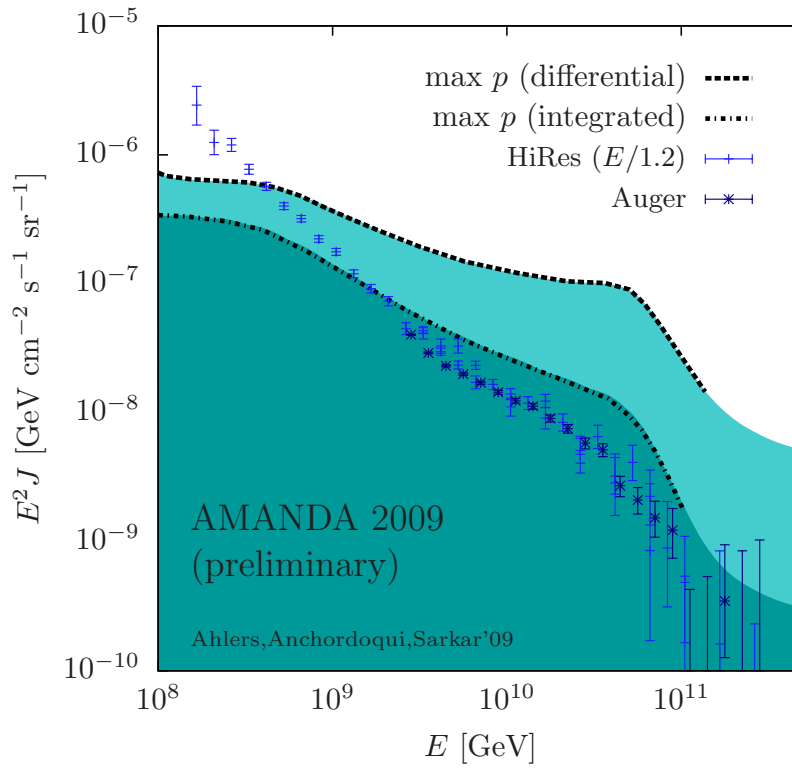


Figure 13: Integrated and differential upper limits on the proton contribution in ultrahigh energy cosmic rays derived from AMANDA bound on diffuse neutrinos (119). (After Ref. (122).)

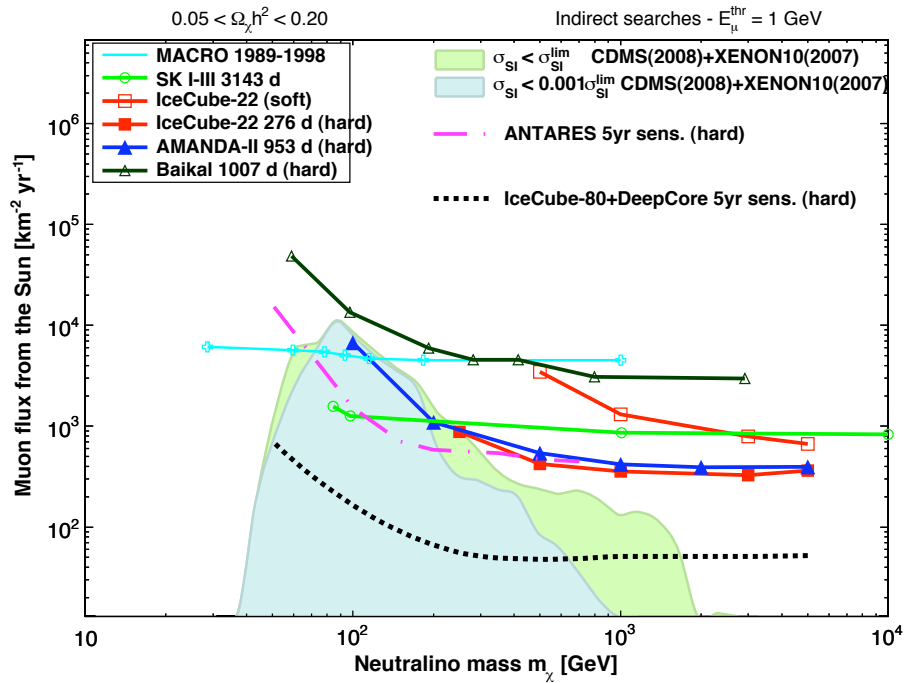


Figure 14: Upper limits (90%CL) on the muon fluxes from neutralino annihilation in the Sun as a function of neutralino mass for soft ($b\bar{b}$) and hard (W^+W^-) channels (85, 147). The lighter hatched region indicates the SUSY parameter space compatible with direct detection limits on the spin independent cross section from CDMS (141) and XENON10 (142). The darker hatched area represents the projected sensitivity for the same region of the parameter space, assuming that direct detection limits are a 100 times better. Experimental limits, that include a correction for detector threshold within the common assumption of $E_{\nu, \text{thr}} = 1$ GeV, are shown for Super-Kamiokande (143), MACRO (144), AMANDA-II (145), Baikal (146) and IceCube 22 strings for the hard and soft channels (147). For comparison, the projected sensitivity of ANTARES after 5 yr of data taken is also shown (148).

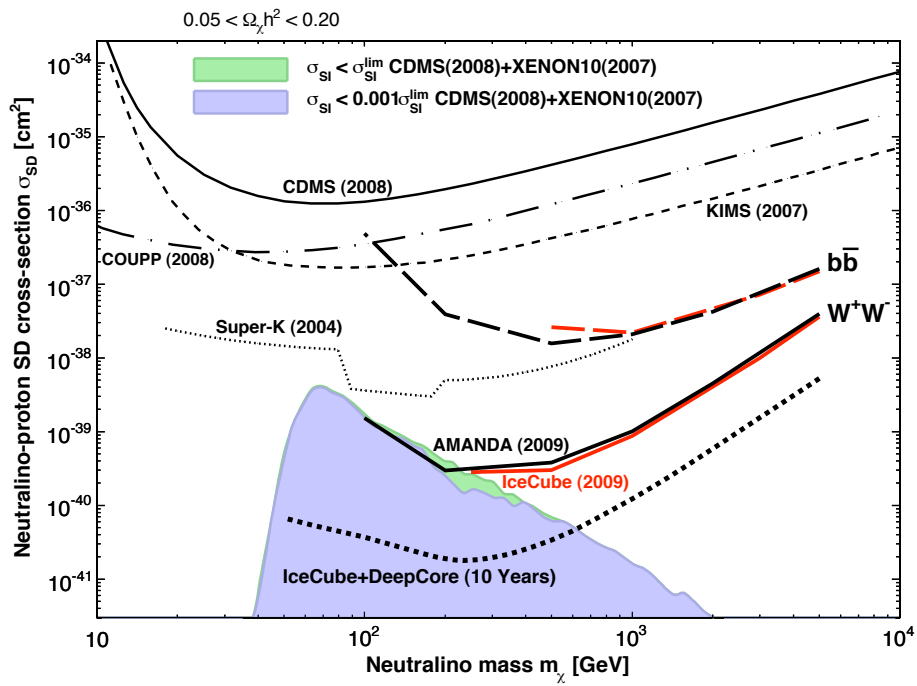


Figure 15: 90% CL upper limits from AMANDA-II and 22 strings of IceCube on the spin dependent cross section for soft and hard channels (147). Hatched regions follow the same conventions of Fig. 14. For comparison, we also show direct search limits on σ_{SD} from CDMS (141), COUPP (149) and KIMS.